SCANNING ELECTRON MICROSCOPY

Copies of transparencies

Vikram Jayaram

OUTLINE

Introduction to scanning probe imaging

- Electron gun and electromagnetic lenses
- Principles of backscattered and secondary electron emission and their dependence on sample composition, topography, voltage, detector position, sample tilt, etc.,
- Resolution and the constraints imposed by aberrations, beam spreading, signal to noise ratio and type of signal
- Other types of signals, including absorbed current, cathodoloumninescence
- Examples of SEM investigations in materials science
- Principles of x-ray emission and detection
- Qualitative and quantitative x-ray analysis for elemental identification and composition
- X-ray mapping, resolution of energy dispersive x-ray spectroscopy (EDAX)
- Electron backscattering patterns: principle, applications for texture and orientation measurements, crystallography in the SEM
- Environmental microscopy, insulating samples
- Modern high resolution capabilities, field emission SEMs, low voltage operation

BOOKS

Scanning electron microscopy and x-ray microanalysis
Goldstein et al., (8 authors)

Scanning electron microscopy
O.C. Wells

Micro structural Characterization of Materials
D. Brandon and W.D. Kaplan

Also look under scanning electron microscopy in the library. The metals Handbook and a book on Fractrography by Hull are additional sources of information on metallurgical aspects.

Conventional Imaging

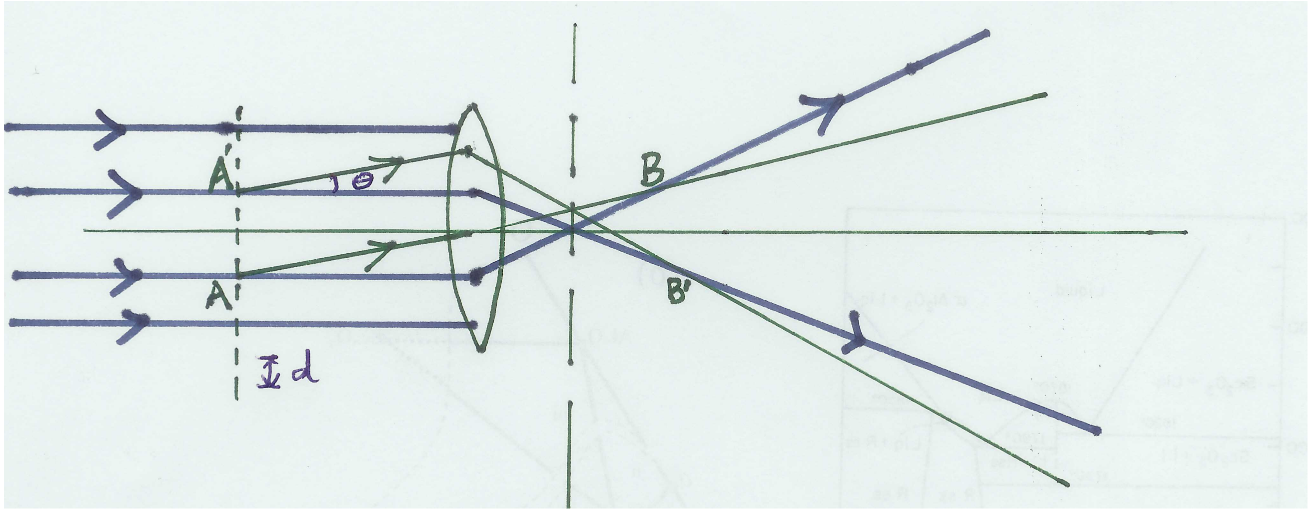

AA' is imaged at BB'. Sin θ ~ λ/d Optically, λ_{min} ~ 0.5 μm, d_{min} ~ 0.3 μm

CONTRAST: Amplitude, Frequency, Phase

DEPTH OF FIELD ~ λ/ Sin θ ~ λ at high magnification, i.e., 0.5 μm

STEREO: Eyes see slightly different images

LIMITATIONS

Poor resolution for many fine scale materials, Poor depth of field,
Need to polish / etch sample, No compositional information

SCANNING PROBE MICROSCOPY

PROBE : Focussed beam of electrons/light, etc
Pointed Tip that SCANS Sample

INTERACTION WITH SAMPLE : Generates Signal [Current, X-rays, Light, Force]

SENSOR : Detects Signal

DISPLAY : Use Signal [direct magnitude or some function] to modulate CRT (TV tube)

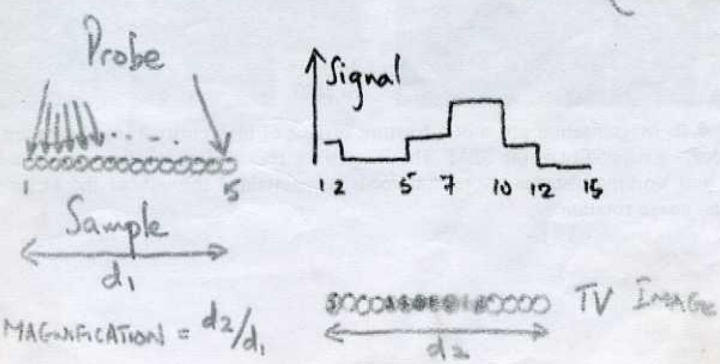

MAGNIFICATION = d_2/d_1

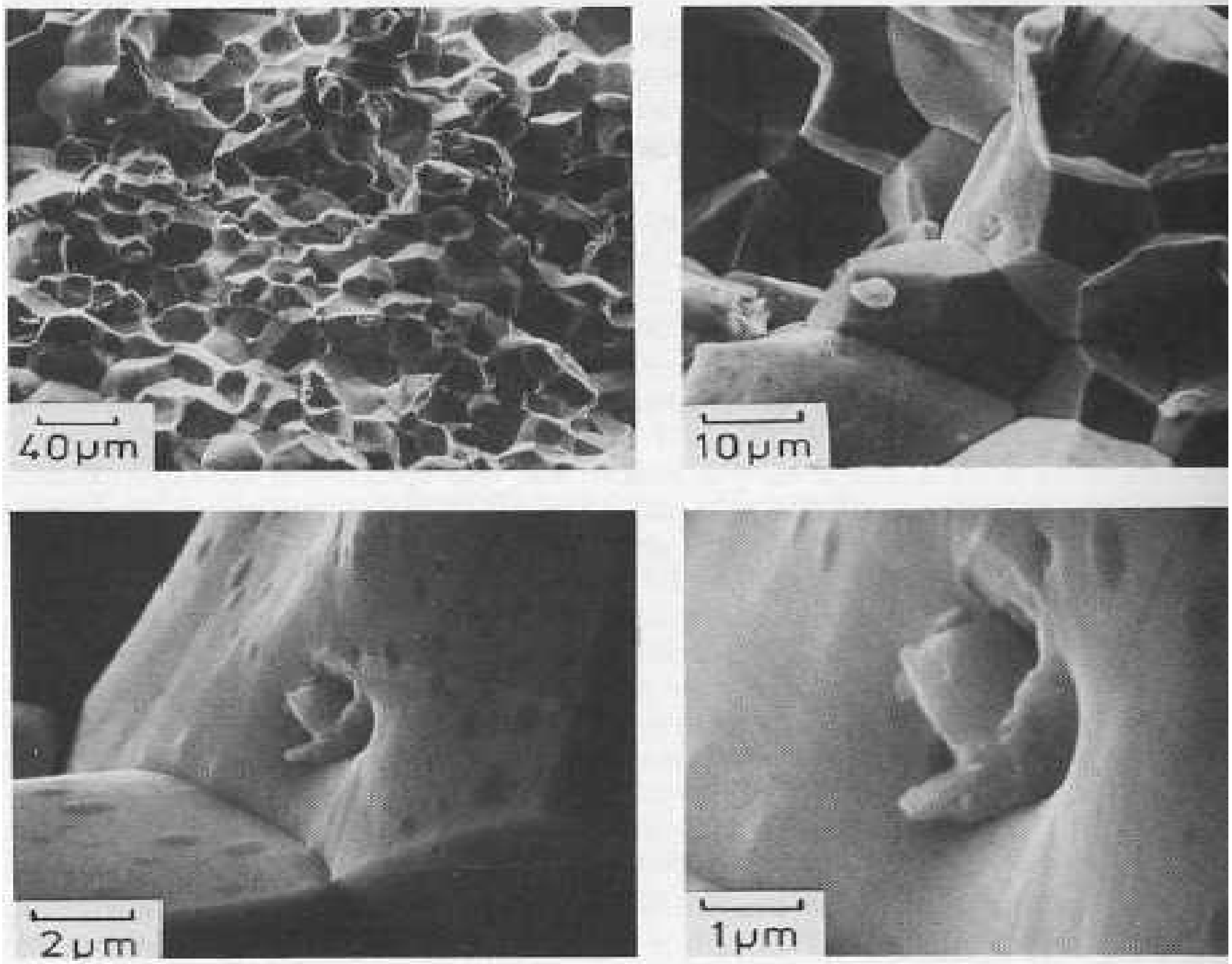

Figure 4.6. Magnification series of a fracture surface of high-purity iron, illustratin rapid surveying capability of the SEM. The images are recorded at constant objective strength and working distance. Note that focus is maintained throughout the serie: there is no image rotation.

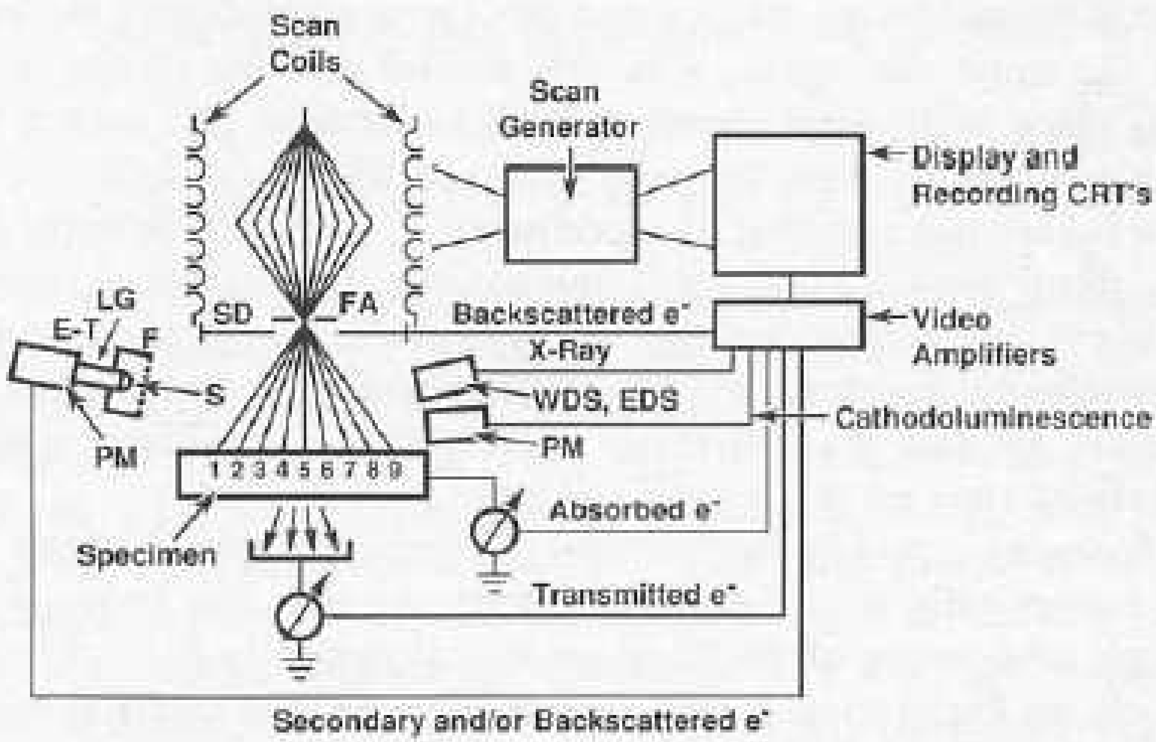

Figure 4.1. Schematic illustration of the scanning system of the SEM. Abbreviations: FA, final aperture; SD, solid-state backscattered-electron detector; EDS, energy-dispersive x-ray spectrometer; WDS, wavelength-dispersive x-ray spectrometer; CRTs, cathode ray tubes, and E–T, Everhart–Thornley secondary/backscattered–electron detector, consisting of F, Faraday cage; S, scintillator; LG, light guide; and PM, photomultiplier. Successive beam positions are indicated by the numbered rays of a scanning sequence.

Table 4.1 Area Sampled as a Function of Magnification[a]

Magnification	Area on sample
10X	$(1\ cm)^2$
100X	$(1\ mm)^2$
1,000X	$(100\ \mu m)^2$
10,000X	$(10\ \mu m)^2$
100,000X	$(1\ \mu m)^2$
1,000,000X	$(100\ nm)^2$

[a] Assumes CRT screen measures 10 cm x 10 cm.

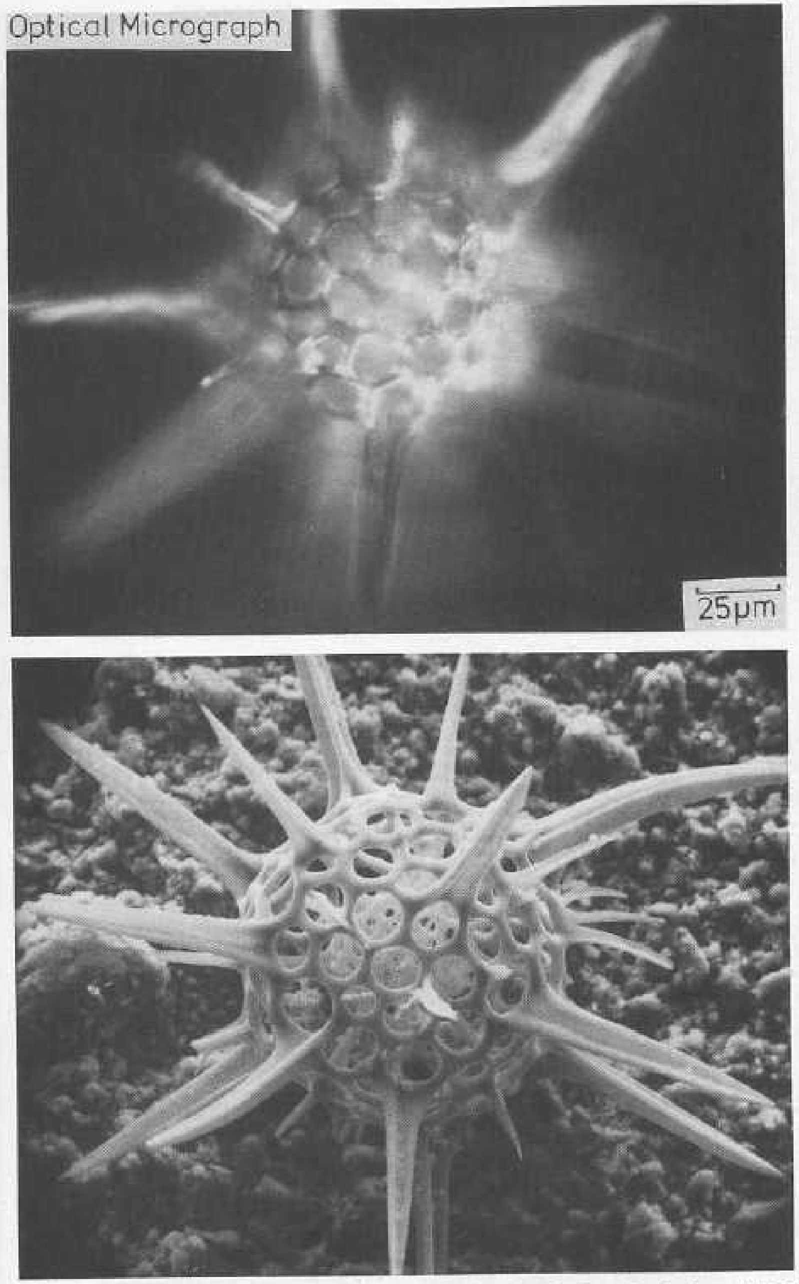

Figure 1.2. (a) Optical micrograph of the radiolarian *Trochodiscus longispinus*. (b) SEM micrograph of same radiolarian. The greater depth of focus and superior resolving capability are apparent.

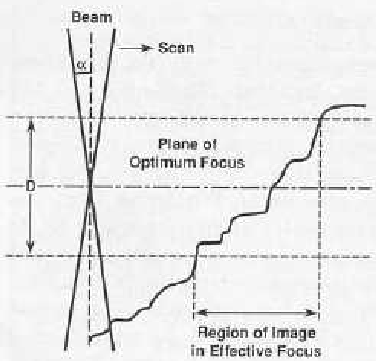

Figure 4.9. Schematic illustration of the depth of focus (field) in a SEM image.

optimum focus. For a sufficiently rough specimen, it is clear from Fig. 4.9 that the beam intersecting some features will become so large that some portion of the specimen will not appear in focus.

To calculate the depth of focus, we must know at what distance above and below the plane of optimum focus the beam has broadened to a noticeable size. The depth-of-focus criterion then depends on where the beam reaches a condition of overlapping adjacent pixels. The geometrical argument in Fig. 4.9 indicates that, to a first approximation, the vertical distance $D/2$ required to broaden the beam of minimum size r_0 to a radius r is given by

$$\tan \alpha = \frac{r}{D/2}. \tag{4.4a}$$

For small angles, $\tan \alpha \approx \alpha$,

$$D/2 \approx r/\alpha \tag{4.4b}$$

$$D \approx 2r/\alpha, \tag{4.4c}$$

where α is the beam divergence, as defined by the semicone angle. Consider that r equals the pixel size of the image. On a high-resolution CRT (spot size = 0.1 mm = 100 μm), most observers will find that defocusing becomes objectionable when two pixels are fully overlapped. The pixel size on the specimen is then given by $0.1/M$ mm, where M is the magnification. Substituting this expression into Eq. (4.4b) gives a practical expression for the depth of focus:

$$D \approx \frac{0.2}{\alpha M} \text{ mm}. \tag{4.4d}$$

Equation (4.4) indicates that to increase the depth of focus D, the operator can choose to reduce either the magnification M or the divergence α. Changing the magnification is not generally an option, since the magnification is chosen to fill the image with the details of interest. This leaves the divergence as the adjustable parameter. The divergence is adjusted by the selection of the final aperture radius, R_{Ap}

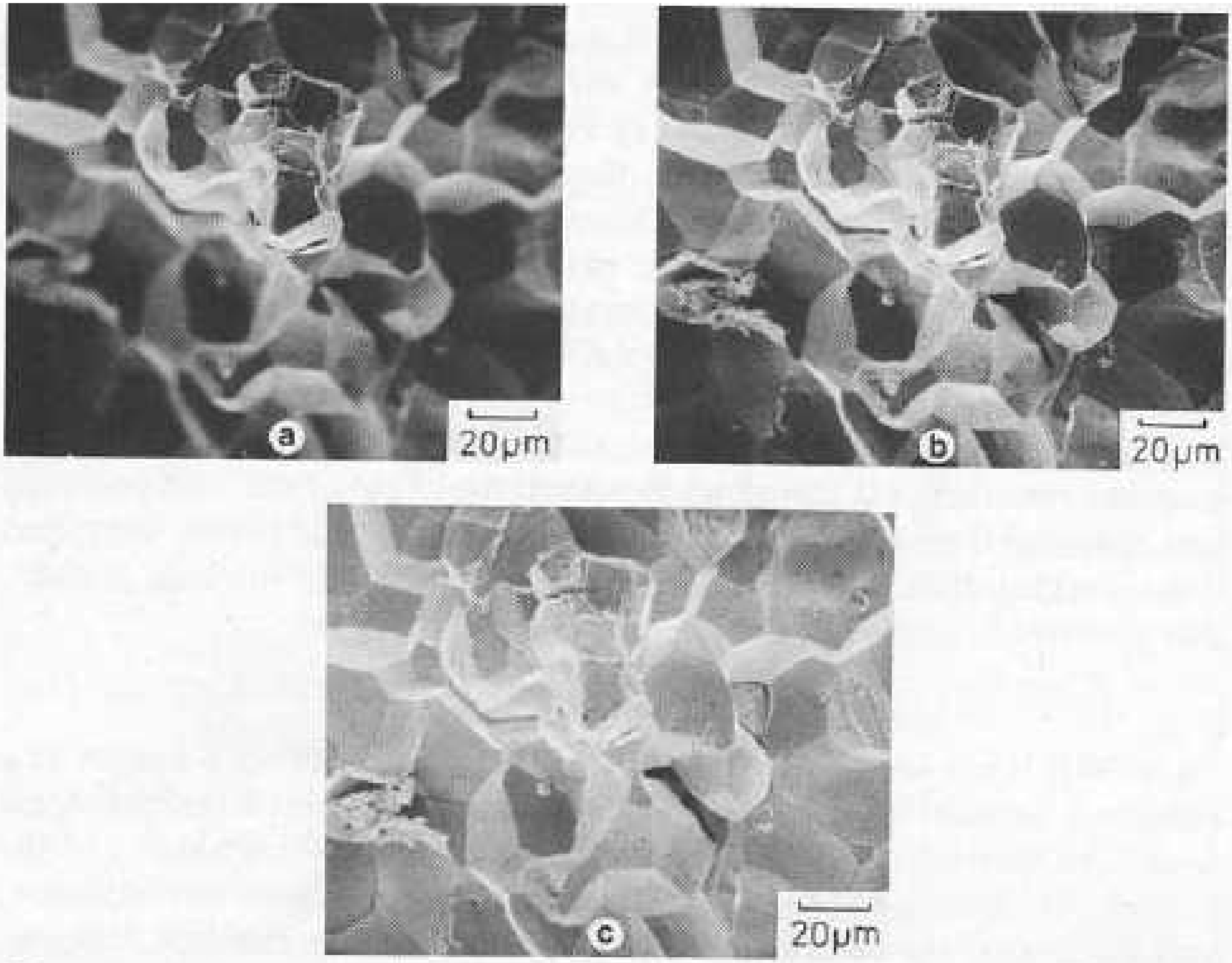

Figure 4.10. Appearance of a fracture surface with different depths of focus obtained by varying the aperture size and the working distance. (a) Small depth of focus, most of the field of view is out of focus (15-mm working distance, 600-μm aperture), (b) Intermediate depth of focus; more of the surface appears in focus (15-mm working distance, 100-μm aperture), (c) maximum depth of focus, entire field in focus (45-mm working distance, 100-μm aperture). Beam energy 20 keV.

Table 4.3. Depth of Focus (Field) in μm

	α (rad)		
Magnification	5×10^{-3}	1×10^{-2}	3×10^{-2}
10X	4,000	2,000	670
50X	800	400	133
100X	400	200	67
500X	80	40	13
1,000X	40	20	6.7
10,000X	4	2	0.67
100,000X	0.4	0.2	0.067

Table 4.2. Size of Picture Element as a Function of Magnification[a]

Magnification	Edge of picture element
10X	10 μm
100X	1 μm
1,000X	0.1 μm (100 nm)
10,000X	0.01 μm (10 nm)
100,000X	1 nm

[a] 1000 × 1000 scan matrix; 10 cm × 10 cm display on CRT.

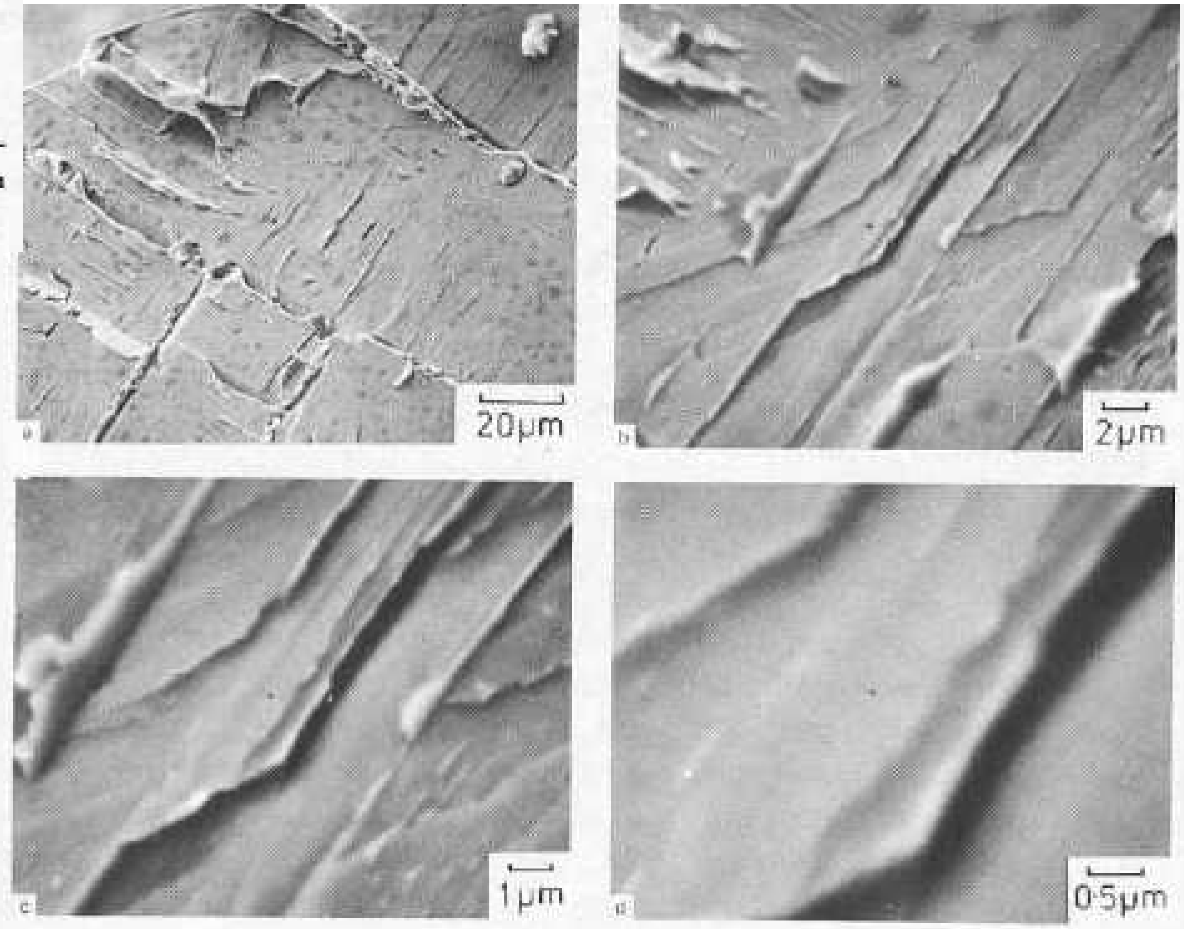

Figure 4.8. Images of a fracture surface illustrating the effects of pixel overlap (hollow magnification). The finest details in the image at low magnification appear sharp, while at the highest magnification, blurring can be observed.

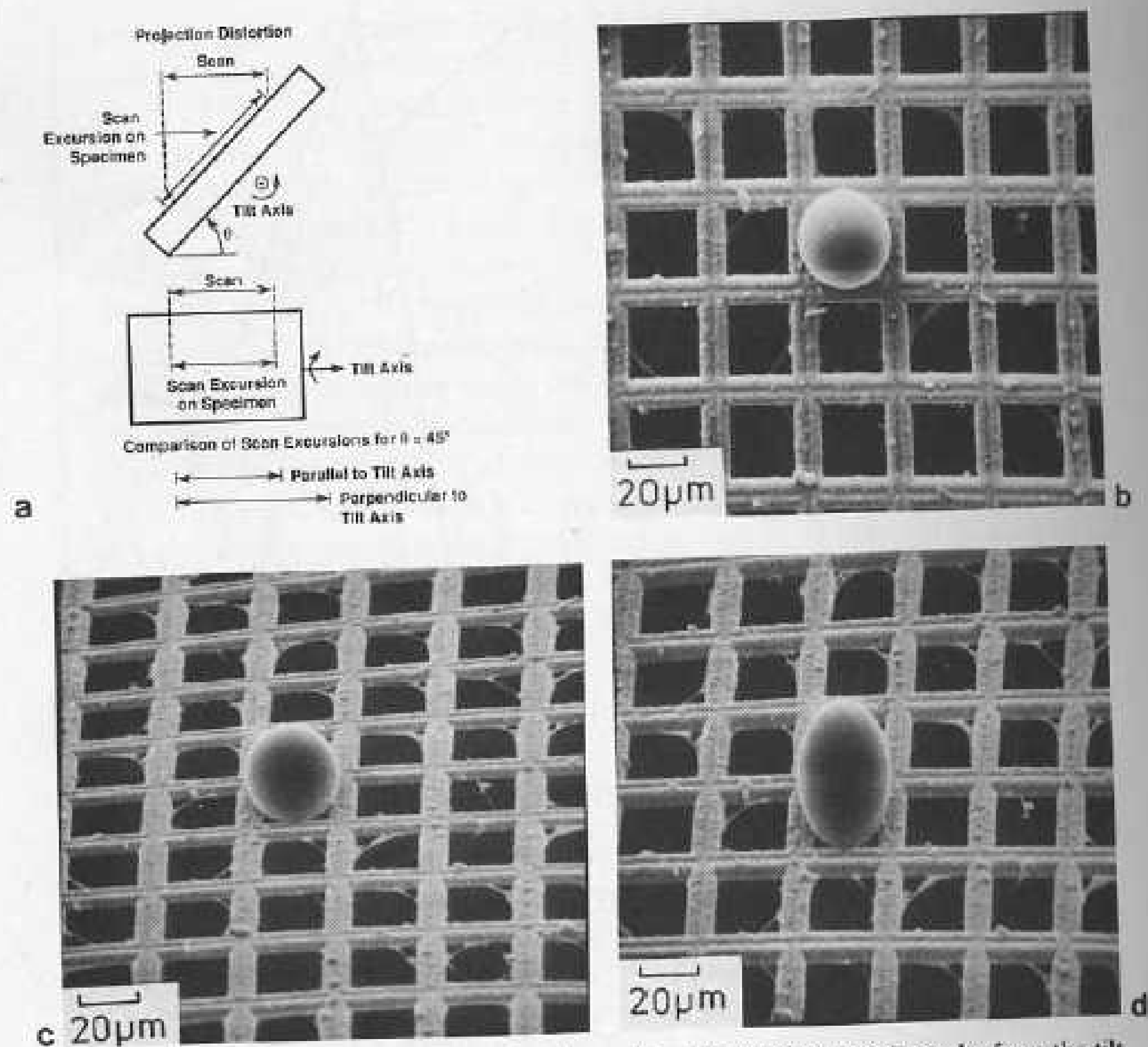

Figure 4.12. (a) Projection distortion (image foreshortening), which results from the tilt of a specimen for a tilt angle of 45°. The scan has the correct length parallel to the tilt axis (horizontal in the displayed image), but is lengthened perpendicular to the tilt axis (vertical in the displayed image), thus reducing the magnification. (b) Latex sphere on a copper grid, specimen plane normal to the beam (0° tilt). (c) Grid-sphere specimen tilted to 55°. (d) Grid-sphere specimen tilted to 55°, tilt correction applied, note restoration of square grid openings, but distortion of sphere.

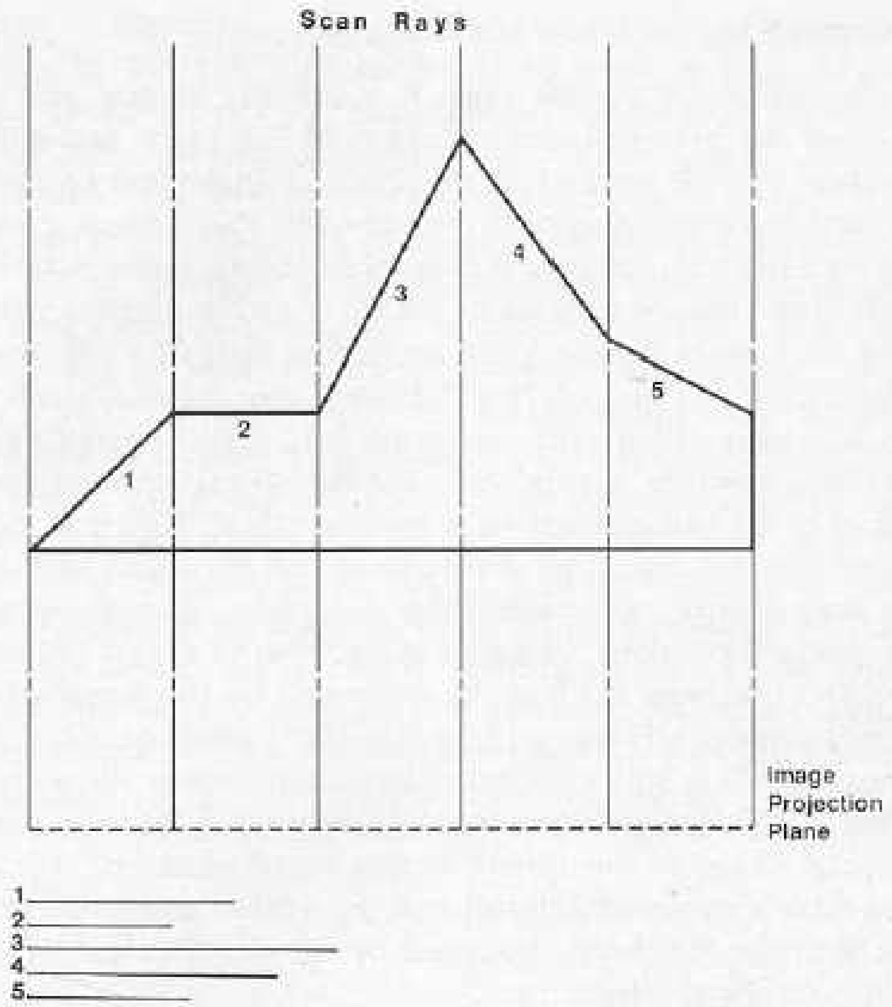

Figure 4.13. Projection distortion of facets with different inclinations to the beam. The magnification is sufficiently high that the scan angle is negligible and the scan rays are nearly parallel to the optic axis. Although the numbered facets have different lengths, their images in projection all have the same apparent length. Below the image projection plane are shown the relative true lengths of the numbered facets.

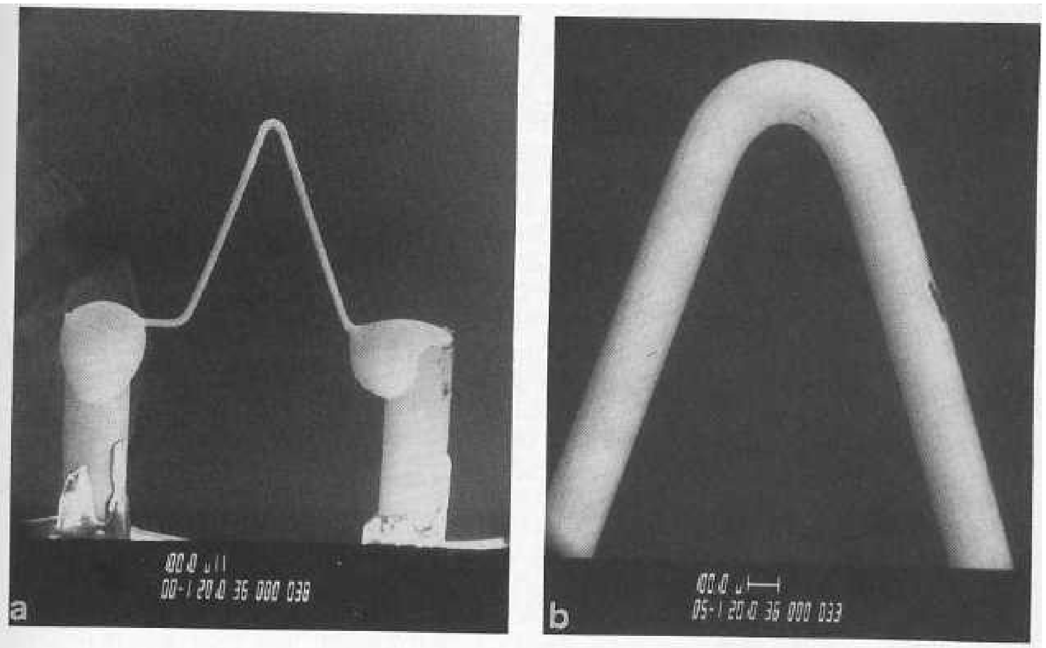

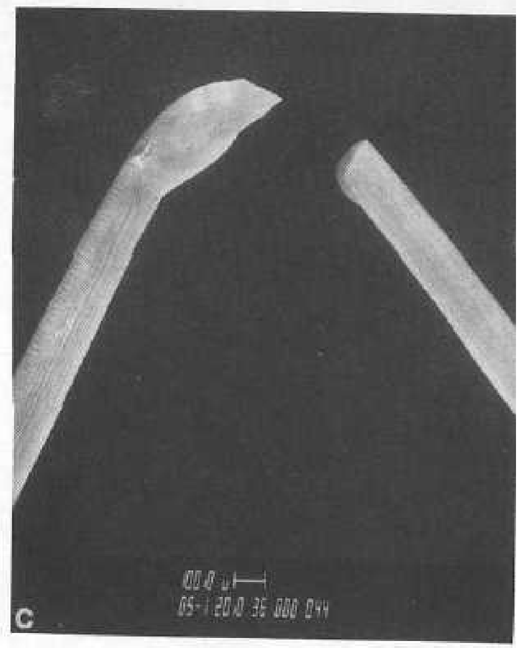

Figure 2.8. SEM micrographs of the tungsten hairpin filament. (a) Filament wire spot-welded to support posts. (b) Tip of wire showing fine wire drawing marks. (c) Filament failure by overheating (oversaturation).

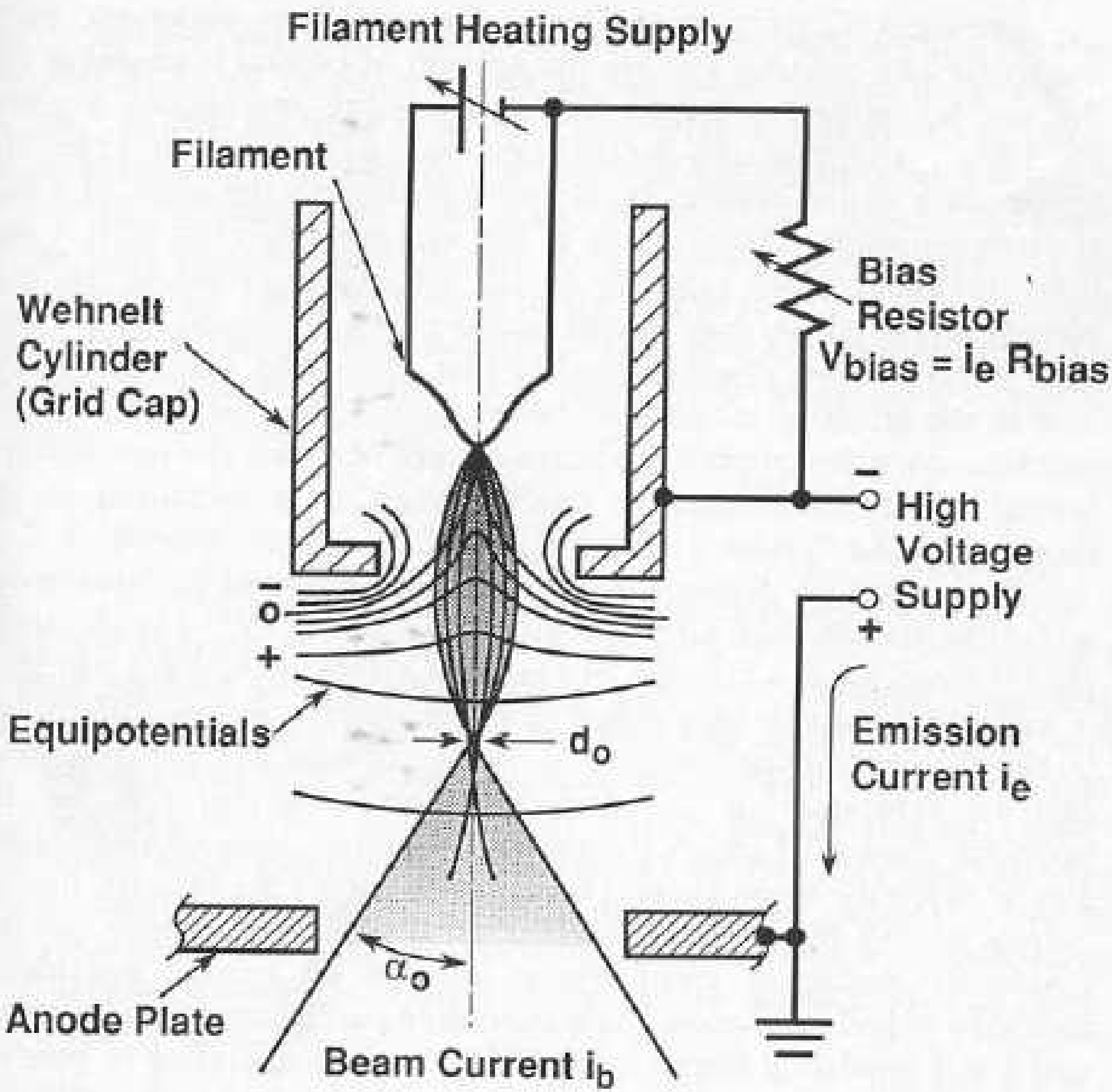

Figure 2.4. Schematic diagram of the conventional self-biased thermionic (triode) electron gun (adapted from Hall, 1966).

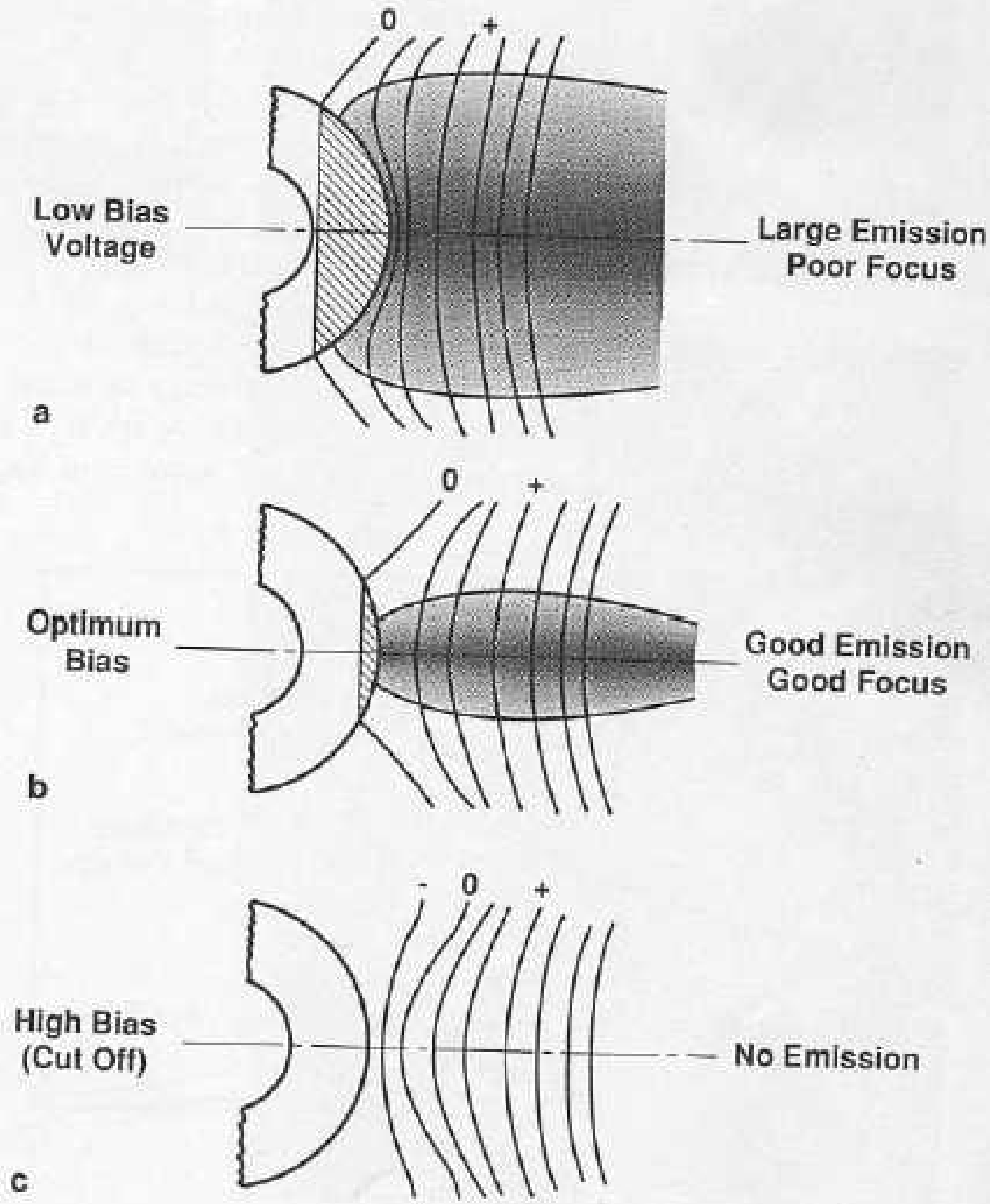

Figure 2.6. Typical emission distributions from the tip of a tungsten hairpin filament for (a) low bias voltage producing high emission but poor focusing, (b) optimum bias voltage producing good focus and good emission, and (c) high bias voltage (cut off) emitting no current (adapted from Haine and Cosslett, 1961).

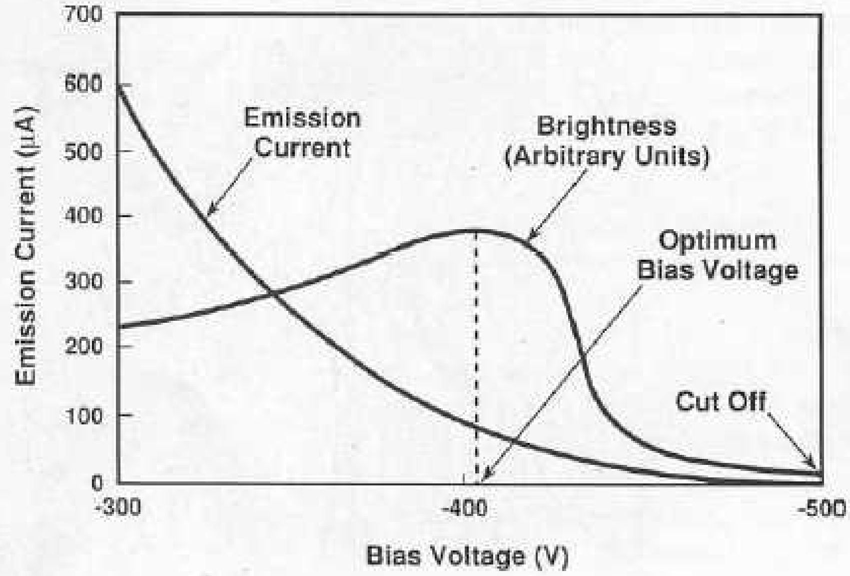

Figure 2.7. Relationship of emission current and brightness to bias voltage. While a brightness maximum should be obtainable in any gun, this schematic diagram shows values and curves for a hypothetical system.

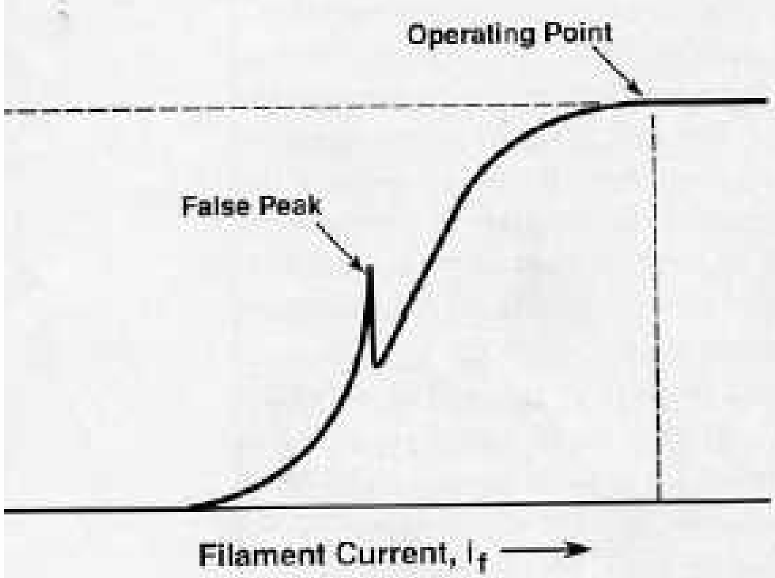

Figure 2.5. Saturation of a tungs pin electron gun. Operating point is of heating current for which no fu crease in beam current can be Usually a false peak is observed ev well-aligned gun. A misaligned gun maximum emission with increased heating current.

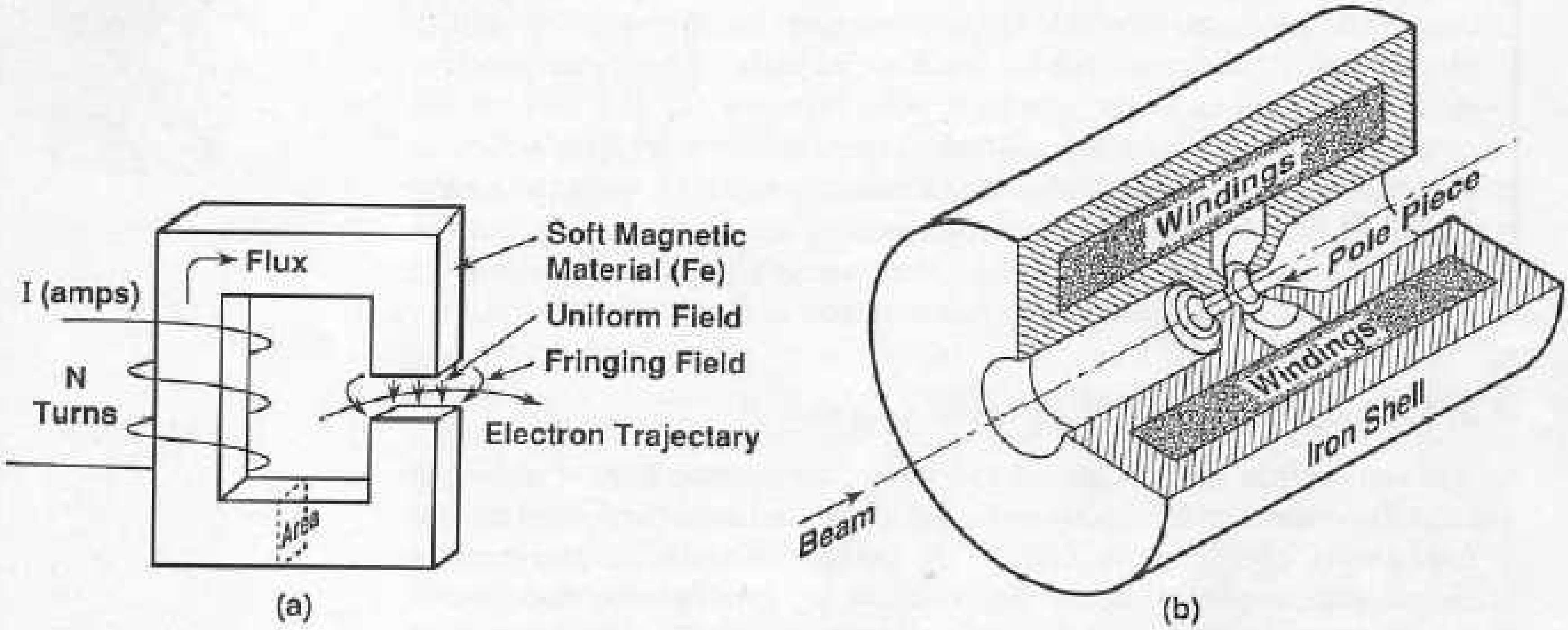

Figure 2.14. Production of a magnetic field inside an electromagnetic lens. (a) A coil of wire energizing a simple magnetic circuit to produce a magnetic field across a gap in the iron circuit. (b) A rotationally symmetric electron lens where the coil windings are inside the iron shroud and the field is produced across the lens gap between polepieces (adapted from Hall, 1966).

the lens parallel to the optic axis and interacts with the radial component $\mathbf{B_r}$. According to the right hand rule of Fig. 2.15c, the vector product $-e(\mathbf{v_z} \times \mathbf{B_r})$ produces a rotational force $\mathbf{F}_{\theta in}$, which in turn gives the electron a rotational velocity $\mathbf{v}_{\theta in}$. This rotational velocity then interacts with the axial component of the $\mathbf{B_z}$ of the field to produce a radial force $\mathbf{F_r} = -e(\mathbf{v}_{\theta in} \times \mathbf{B_z})$ on the electron. This radial force causes the electron's trajectory to curve toward the optic axis and cross it. The focal length f of the lens is the distance along the optic axis from the point where an electron first changes direction to the point where the electron

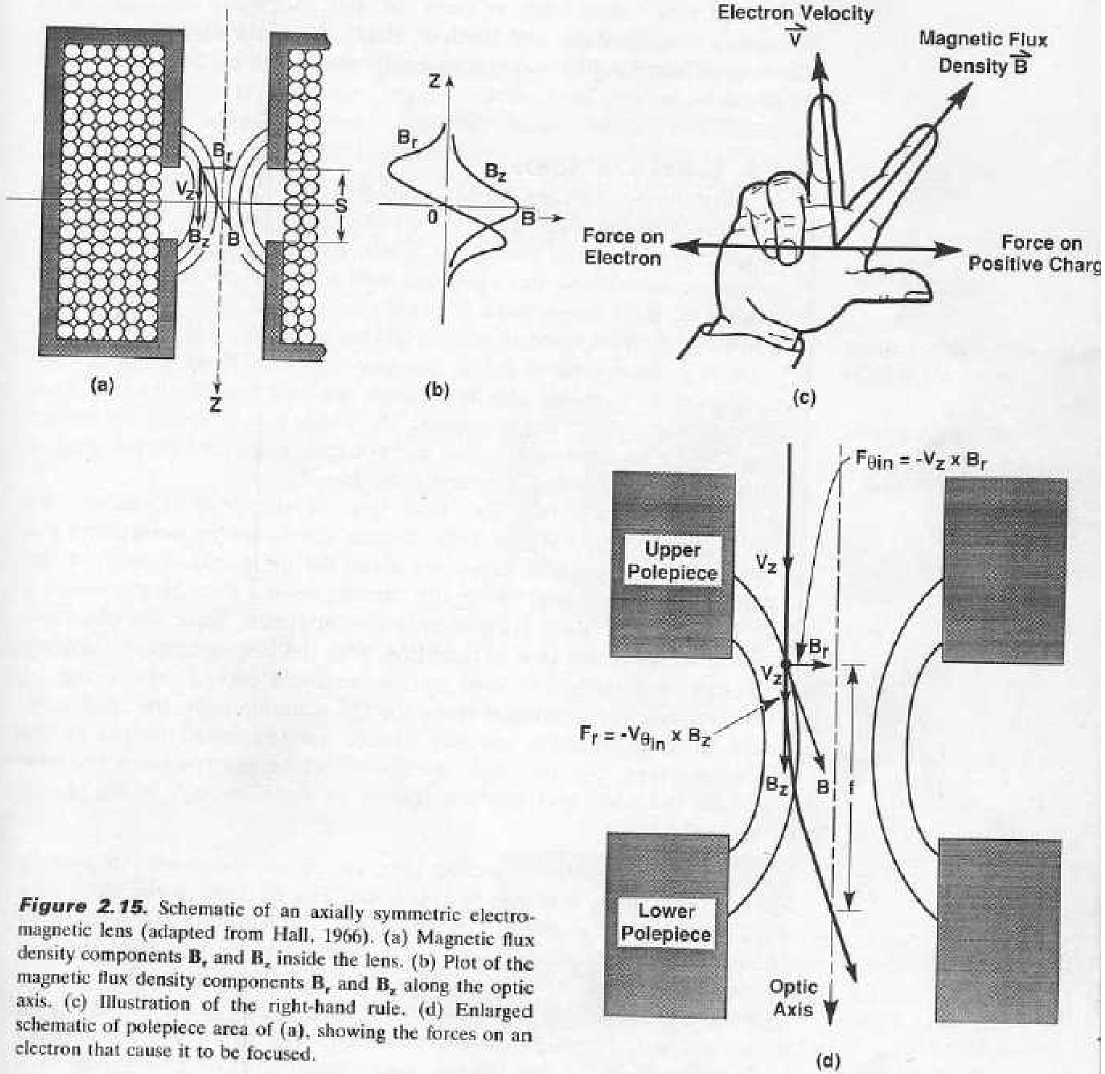

Figure 2.15. Schematic of an axially symmetric electromagnetic lens (adapted from Hall, 1966). (a) Magnetic flux density components $\mathbf{B_r}$ and $\mathbf{B_z}$ inside the lens. (b) Plot of the magnetic flux density components $\mathbf{B_r}$ and $\mathbf{B_z}$ along the optic axis. (c) Illustration of the right-hand rule. (d) Enlarged schematic of polepiece area of (a), showing the forces on an electron that cause it to be focused.

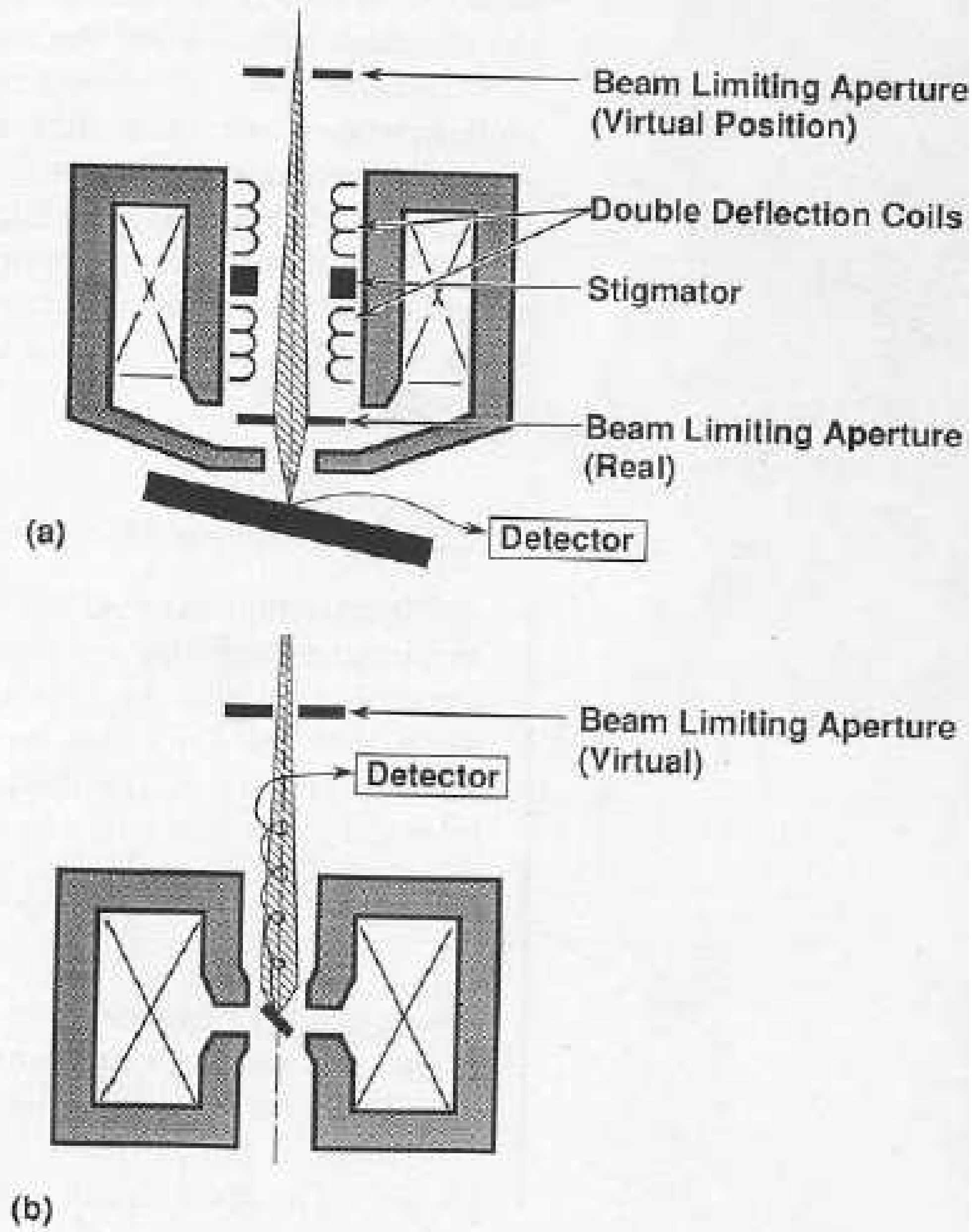

Figure 2.16. Two objective lens configurations. (a) Asymmetrical pinhole lens or conical lens, allowing a large specimen to be placed outside the lens. (b) Symmetrical immersion lens, where a small specimen is placed inside the lens.

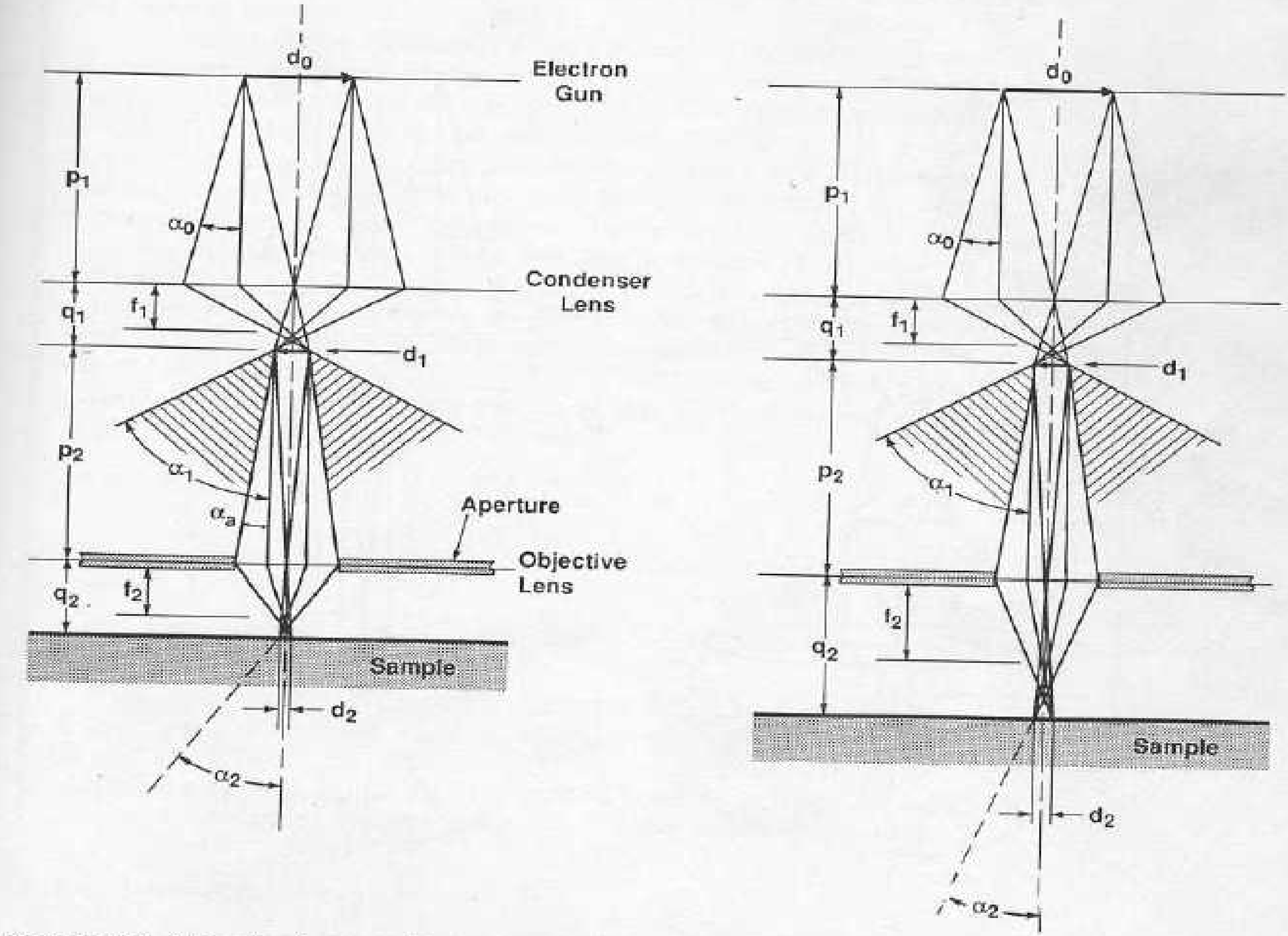

Figure 2.19. Schematic of ray traces for two-lens probe forming system. (a) Small working distance. (b) Large working distance.

decreases, giving rise to an improved depth of field. To obtain this focusing condition at large W, the objective lens current must be decreased, which in turn increases the focal length f_2 of the lens. This increased working distance also increases the scan length that the beam traverses on the specimen. Thus, long working distances can be used to obtain very low magnifications. Finally, by considering Fig. 2.19, one can understand the alternate method of focusing whereby the working distance is selected by setting the current in the objective lens and the operator physically moves the specimen vertically along the z-axis until it comes into focus on the screen.

Effect of Condenser Lens Strength. Increasing the strength of the condenser lens decreases both the final probe size $d_p = d_2$ and the amount of current i_p in the final probe, as shown in Fig. 2.20. With a constant working distance and objective lens aperture size, an increase

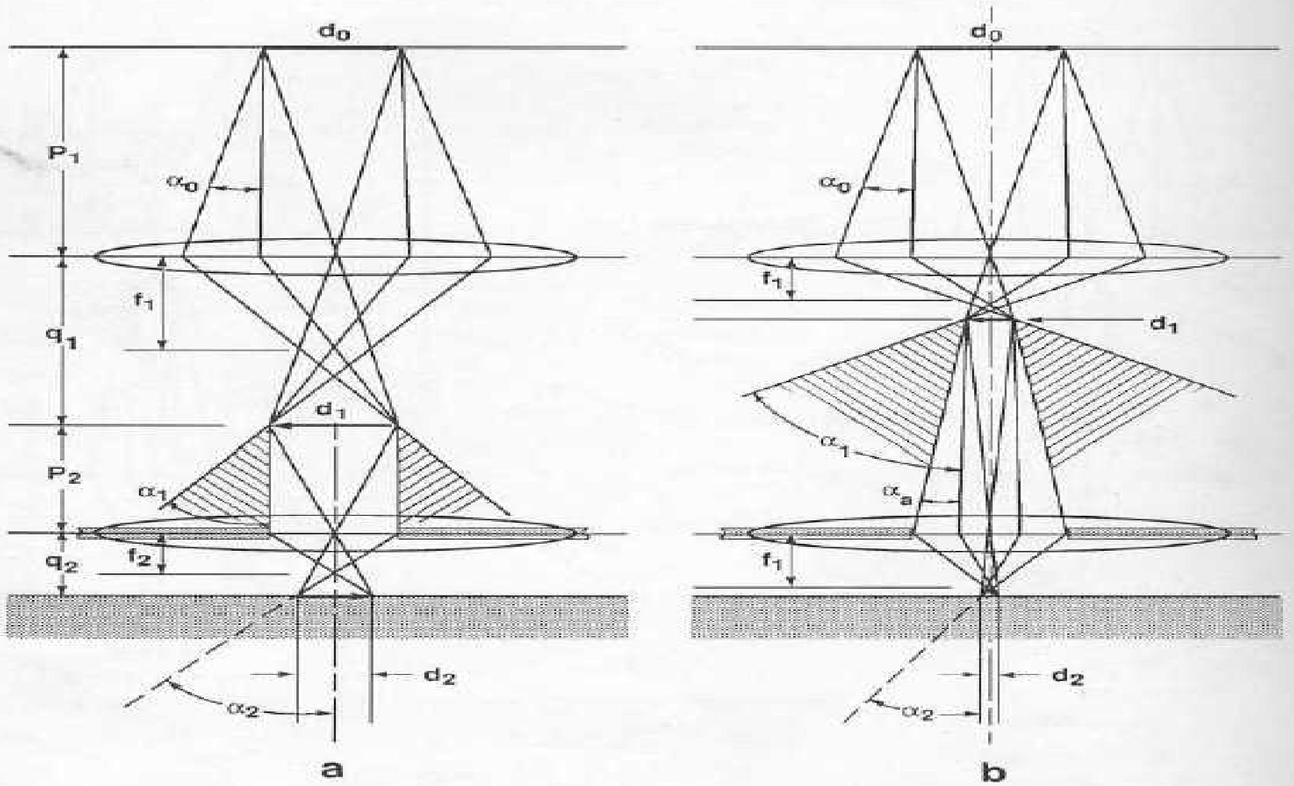

Figure 2.20. Schematic of ray traces for two-lens probe forming system: (a) weak condenser lens, (b) strong condenser lens.

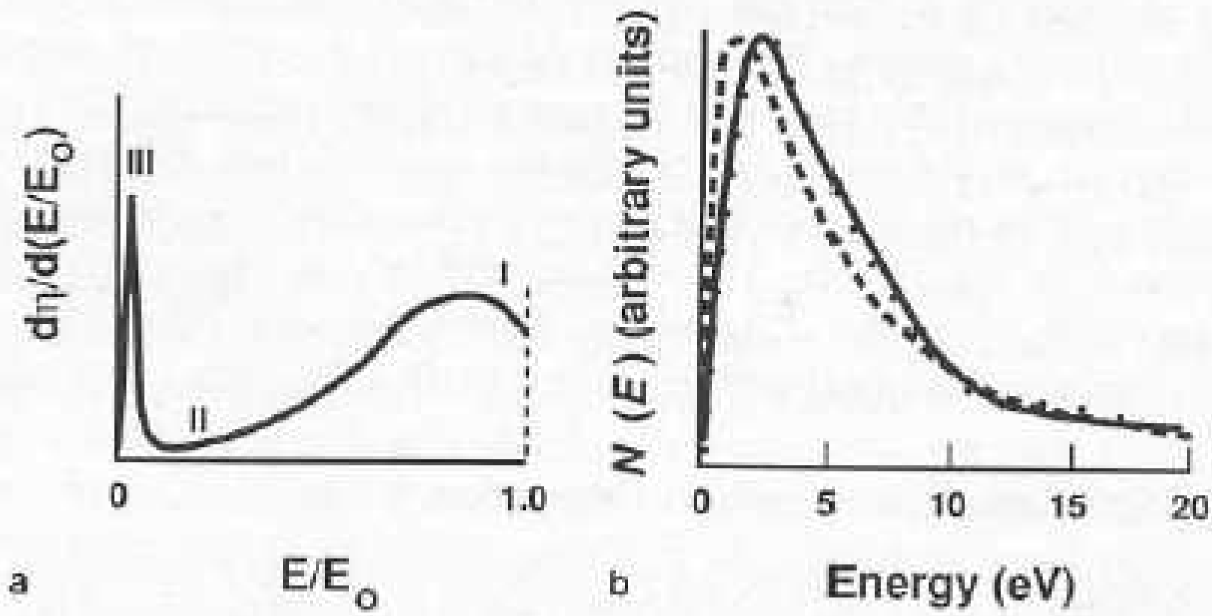

Figure 3.25. (a) Complete energy distribution of electrons emitted from a target, including backscattered electrons (regions I and II) and secondary electrons (region III). Note that the width of region III is exaggerated. (b) Secondary-electron energy distribution as measured (points) and as calculated (lines) with different assumptions on secondary propagation (Koshikawa and Shimizu, 1974).

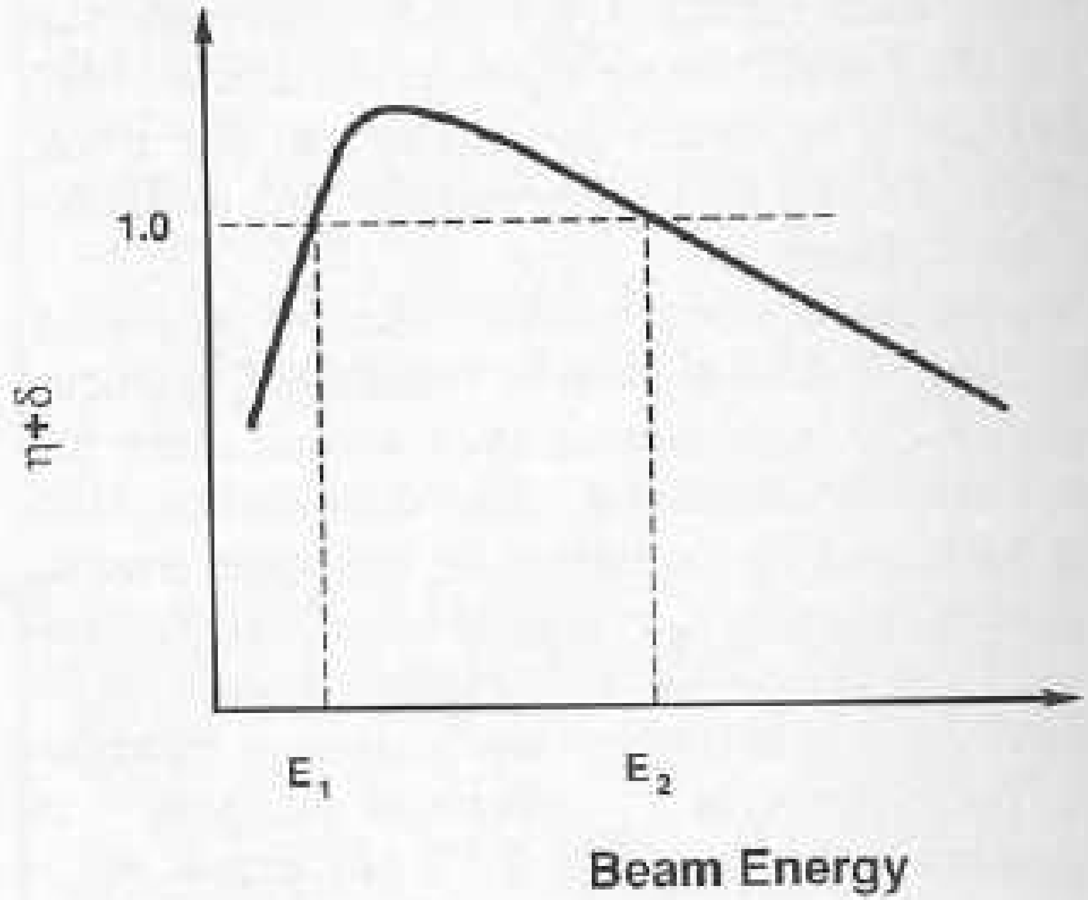

Figure 3.27. Total emitted-electron coefficient $\eta + \delta$ as a function of beam energy.

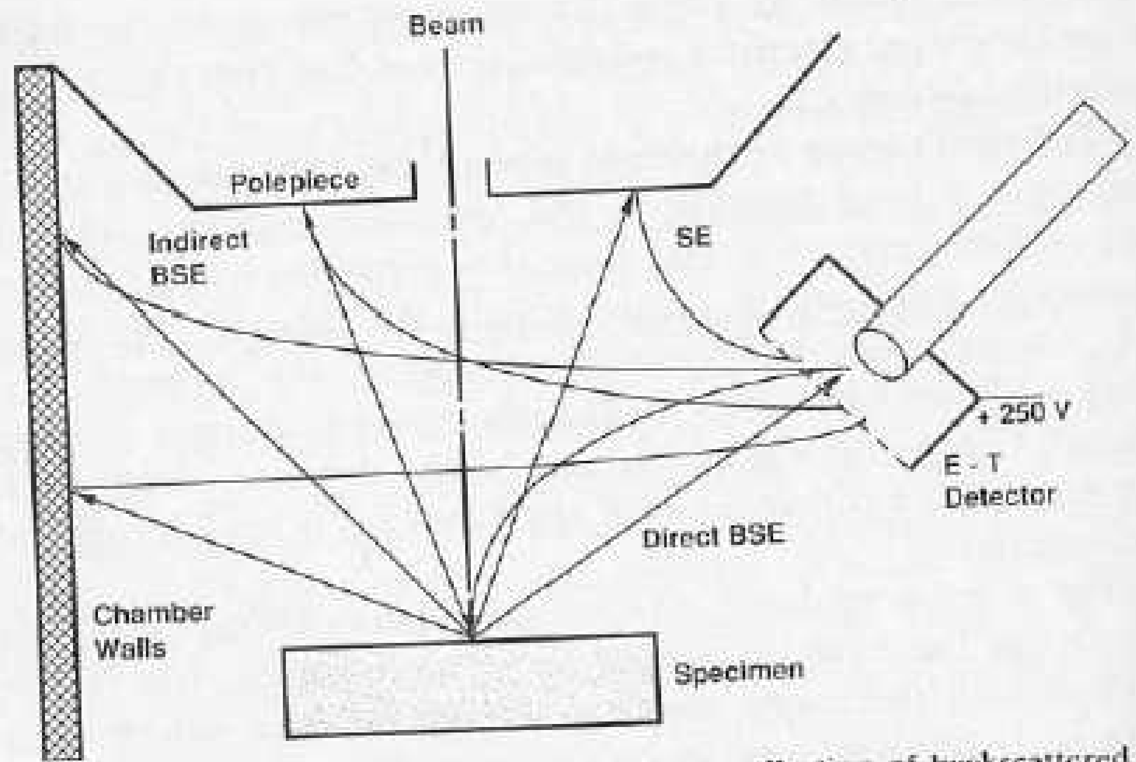

Figure 4.21. Schematic illustration of the indirect collection of backscattered electrons by a positively biased E–T detector. The backscattered electrons strike the polepiece and chamber walls, where they create secondary electrons. These secondaries are collected by the E–T detector with high efficiency. Although nominally a contribution to the secondary signal, they really represent the backscattered-electron signal component.

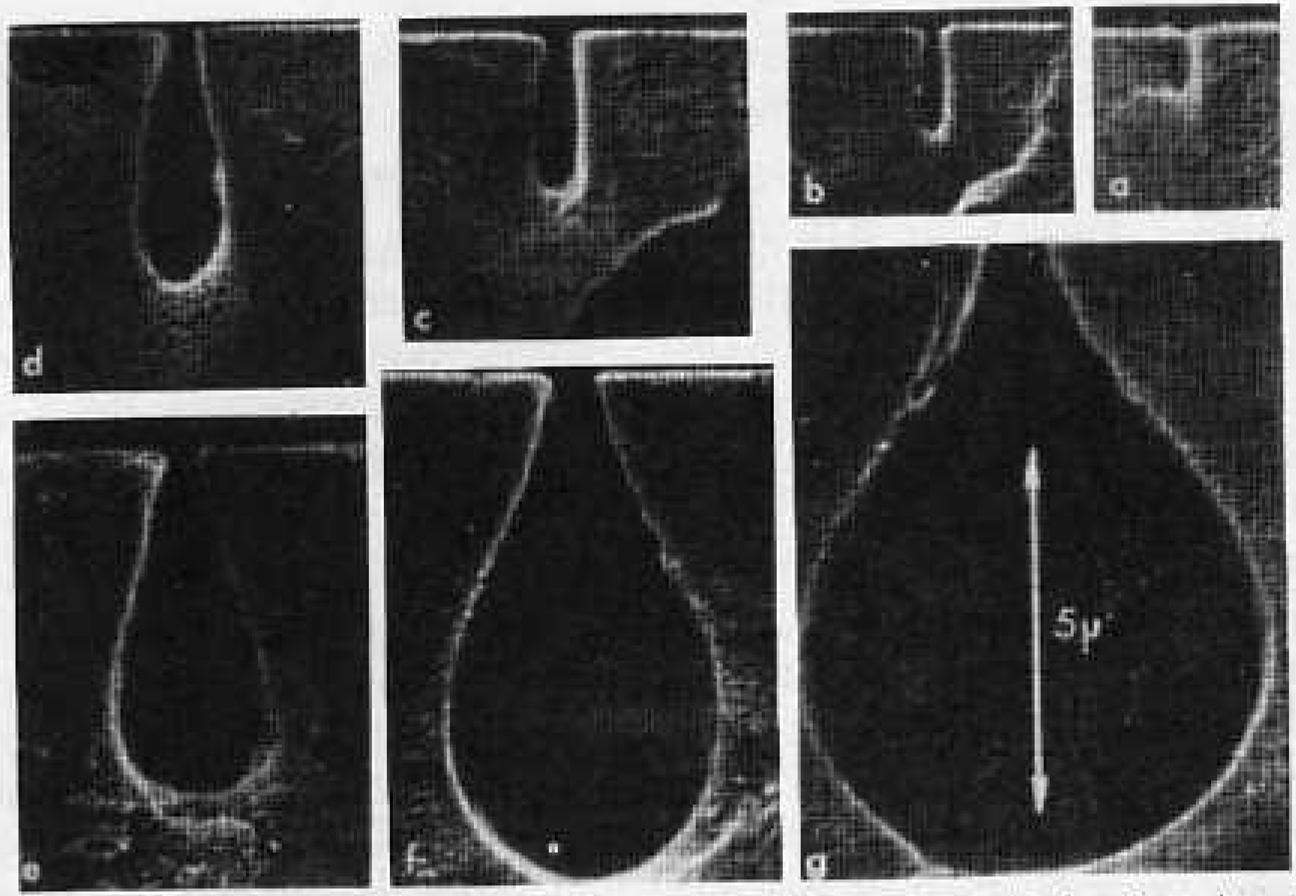

Figure 3.5. Direct visualization of the electron volume in polymethylmethacrylate. In (a) through (g), the electron dose is the same, but the etching time is increased progressively to reveal successively lower energy deposition (radiation damage) levels (from Everhart *et al.*, 1972).

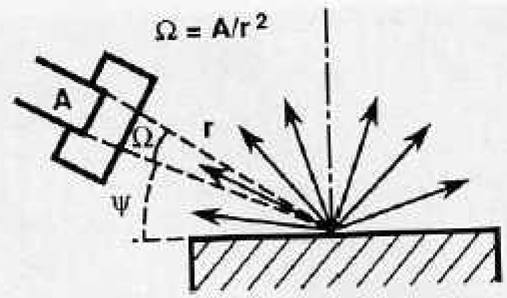

Figure 4.17. General characteristics of detectors. The position of the detector relative to the beam and the specimen is described by the take-off angle, ψ. The size of the detector is given by the solid angle Ω, which is equal to the area of the detector divided by the square of the radial distance to the beam impact point, $\Omega = A/r^2$.

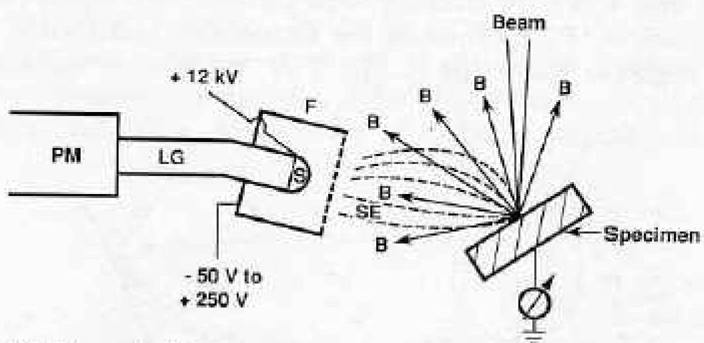

Figure 4.18. Schematic diagram of the Everhart–Thornley detector: B, backscattered-electron trajectories; SE, secondary-electron trajectories; F, Faraday cage (bias range −50 V to +250 V); S, scintillator, with thin metallic coating; high bias (+12 kV) supply to the scintillator coating; LG, light guide; PM, photomultiplier.

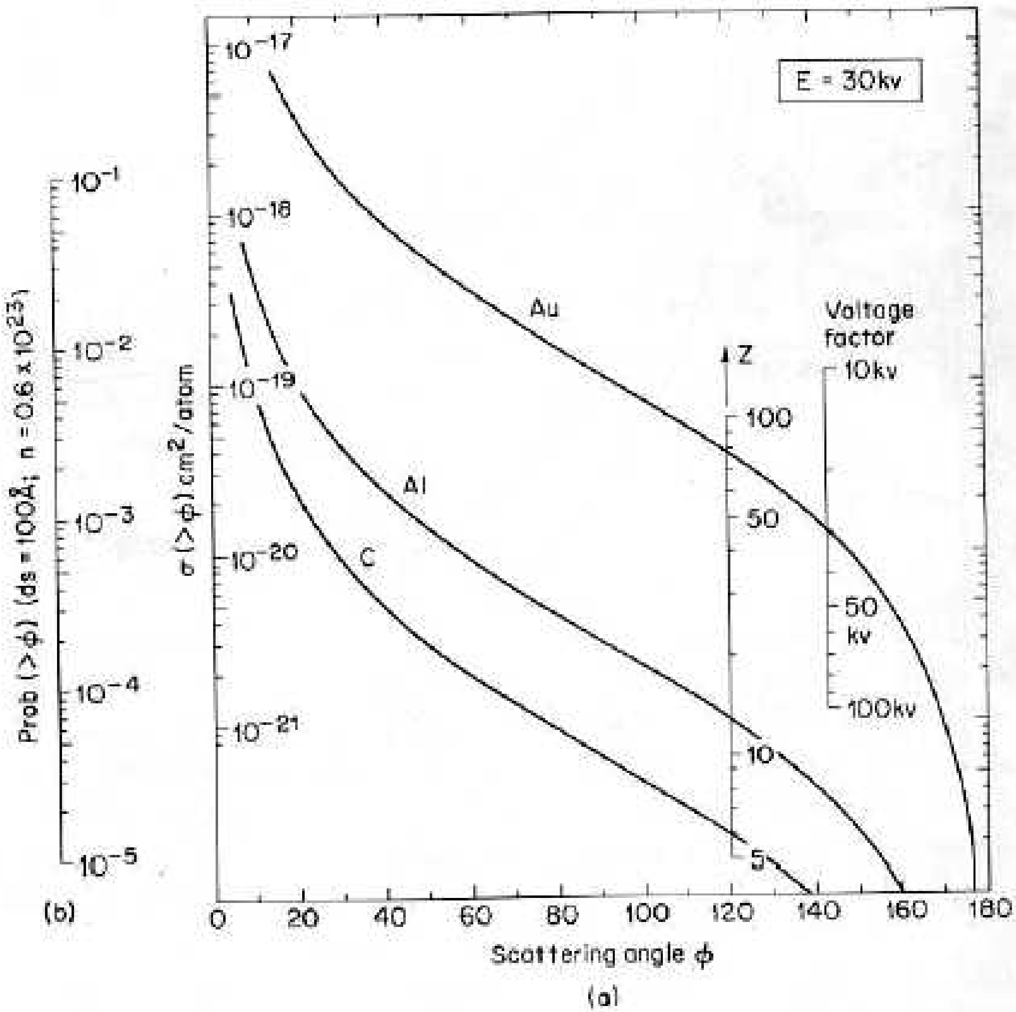

FIG. 3.1 (*a*) Total Rutherford scattering cross section for C, Al, and Au at 30 kv; (*b*) probability of a Rutherford scattering event through an angle $> \phi$ for a path element of length 100 Å.

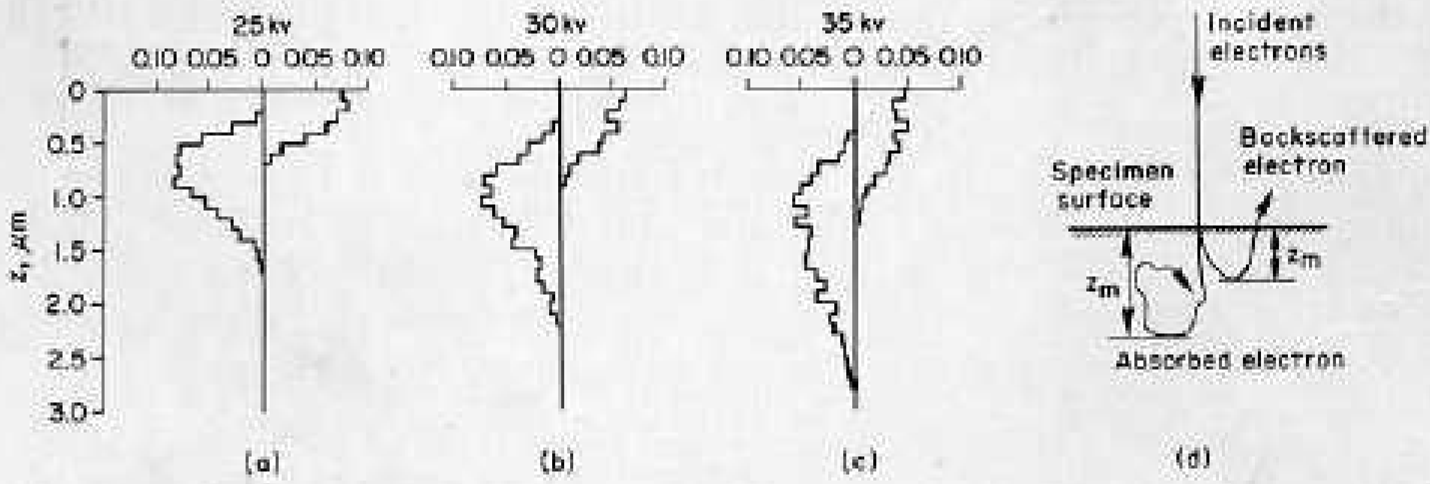

FIG. 3.4 (*a*), (*b*), and (*c*) Distribution of maximum penetration depth for backscattered (right-hand side) and absorbed (left-hand side) electrons in copper specimen as calculated by the Monte Carlo method; (*d*) definitions of depth. (*Shinoda, Kawabe, Murata, and Shirai 1966. Courtesy of Tech. Rep. Osaka Univ.*)

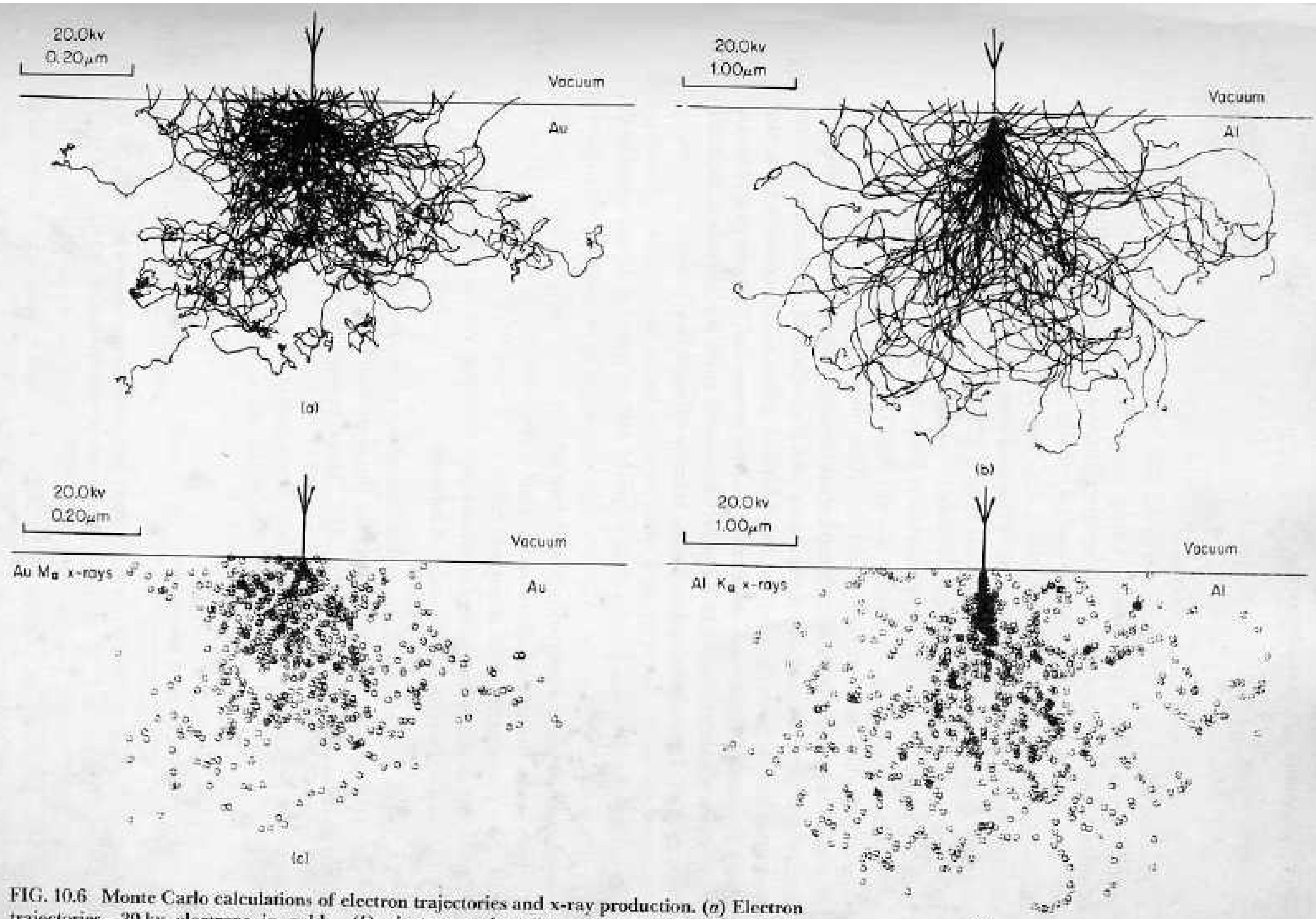

FIG. 10.6 Monte Carlo calculations of electron trajectories and x-ray production. (*a*) Electron trajectories—20 kv electrons in gold; (*b*) electron trajectories—20 kv electrons in aluminum; (*c*) x-ray production—20 kv, Au M_α; (*d*) x-ray production—20 kv, Al K_α. (*Courtesy of R. B. Bolon, General Electric Corporate Research and Development Center.*)

MAXIMUM BRIGHTNESS $= \dfrac{J_c\, eV_0}{\pi kT}$

[current density / solid angle]

where $J_c = 120\,T^2 e^{-E_W/kT}$ Amp. cm^{-2}

W – typical: 2700 K, 20 kV → 10^5 A/cm^2 ster

KANAYA – OKAYAMA RANGE

$$R_{KO} = \frac{0.0276\, A\, E_0^{1.67}}{Z^{0.89}\rho}$$
(μm)

E_0 (keV), A = gram·mol (Atomic Wt.)
ρ = density g cm^{-3}, Z = Atomic No.

Tilted Sample: $R_{KO}(\theta) = R_{KO} \cos\theta$

(e.g) R_{KO} at	C	Al	Cu	Au
5 kV =	0.5	0.4	0.14	0.085
20 kV =	5.3	4.2	1.5	0.86

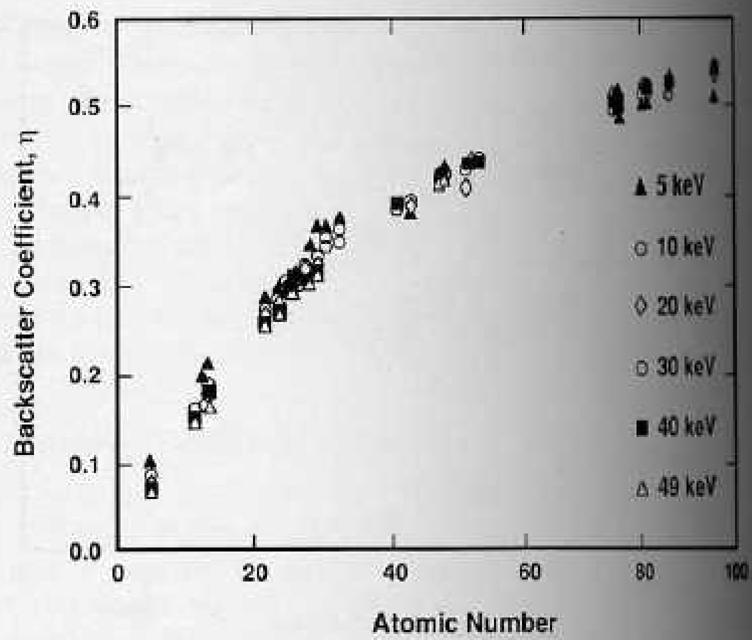

Figure 3.15. Backscattered-electron coefficient as a function of atomic number plotted for a range of beam energies from 5 keV to 49 keV [data of Bishop (1966) and Heinrich (1966a)].

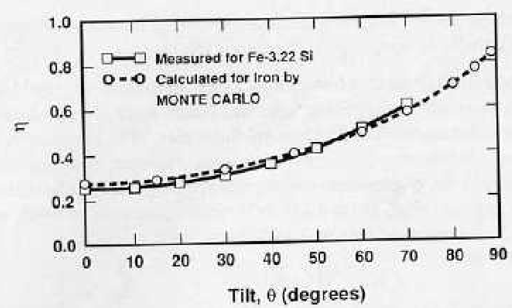

Figure 3.16. Backscattered-electron coefficient as a function of tilt as measured for iron–silicon and as calculated by Monte Carlo electron-trajectory simulation (Newbury *et al.*, 1973).

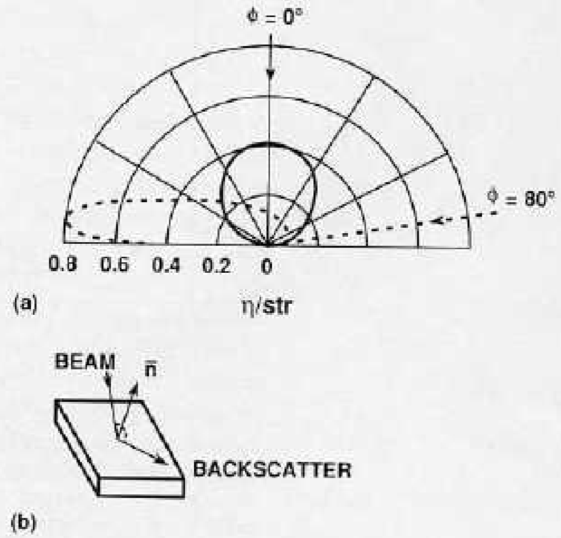

Figure 3.20. (a) Comparison of the angular distribution of backscattered electrons for sample tilts of $\theta = 0°$ and $\theta = 80°$. Note that the angular distribution is strongly peaked in the forward direction at high tilt. (b) Schematic illustration of the direction of maximum backscattering in a highly tilted specimen; the backscatter maximum tends to be in a plane defined by the incident-beam vector and the surface normal.

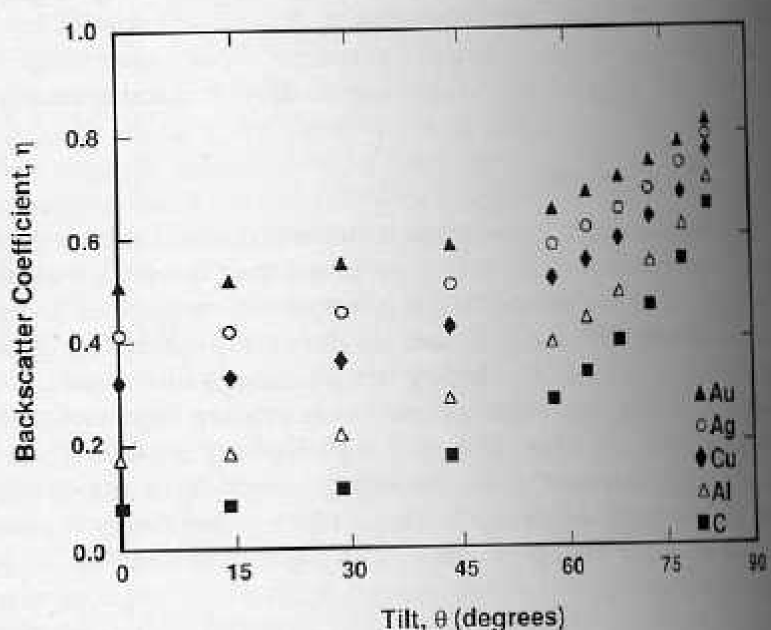

Figure 3.17. Backscattered-electron coefficient as a function of tilt as calculated for several elements by Monte Carlo electron-trajectory simulation (20 keV).

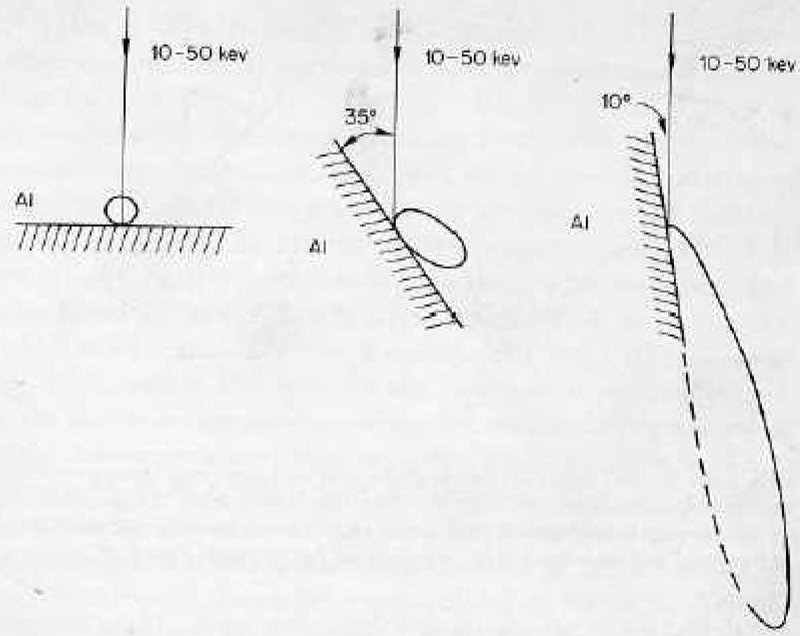

FIG. 3.9 Angular distribution of backscattered electrons with oblique incidence. (*Data from Kanter 1957.*)

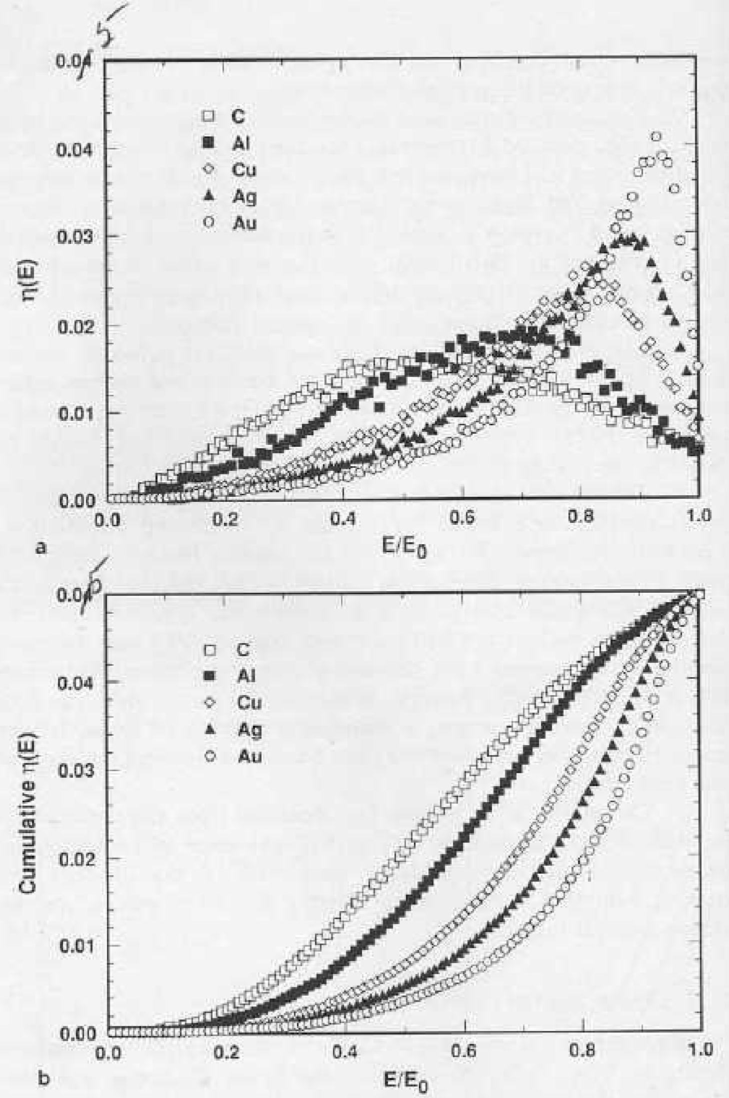

Figure 3.22. Monte Carlo electron-trajectory simulations for the energy distribution of backscattered electrons emitted into 2π steradians (Newbury and Myklebust, 1991): **(a)** $\eta(E)$ vs E/E_0; **(b)** cumulative $\eta(E)$ distribution.

Table 3.3. Backscattered-Electron Energy Distribution (E/E_0)

	Cumulative Fraction Reached		
Element	>0.5	>0.75	>0.9
Carbon	0.55	0.72	0.85
Aluminum	0.63	0.77	0.87
Copper	0.74	0.83	0.92
Silver	0.79	0.88	0.94
Gold	0.84	0.92	0.96

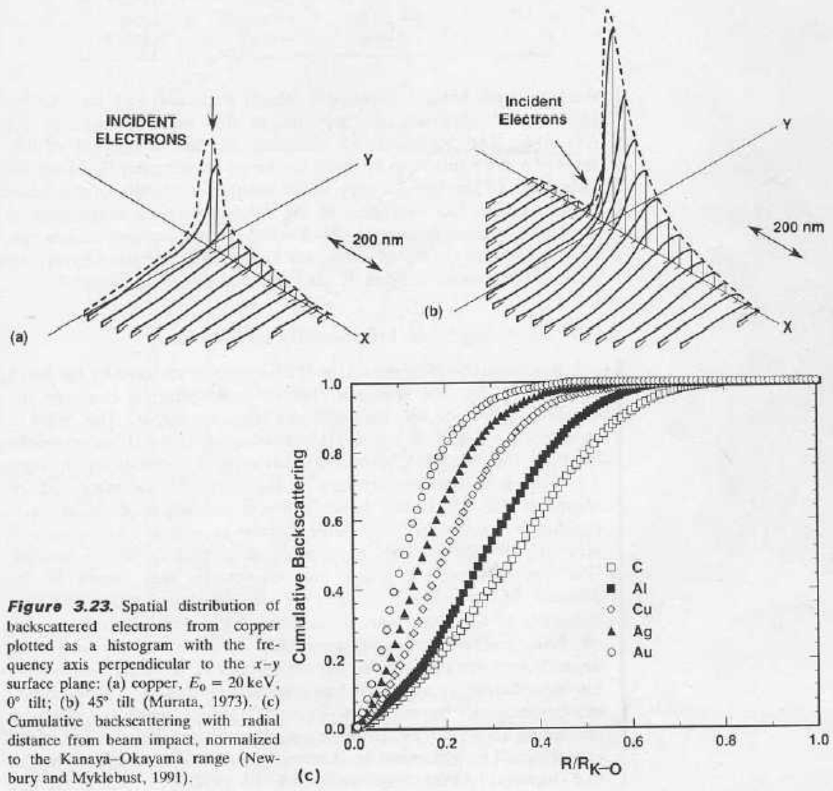

Figure 3.23. Spatial distribution of backscattered electrons from copper plotted as a histogram with the frequency axis perpendicular to the x–y surface plane: (a) copper, $E_0 = 20$ keV, 0° tilt; (b) 45° tilt (Murata, 1973). (c) Cumulative backscattering with radial distance from beam impact, normalized to the Kanaya–Okayama range (Newbury and Myklebust, 1991).

Table 3.4. Cumulative Radial Backscattering (20 keV)

a. Distribution Fraction

Element	80%	90%	95%
C	0.502	0.575	0.63
Al	0.419	0.490	0.545
Cu	0.318	0.382	0.439
Ag	0.250	0.310	0.365
Au	0.195	0.248	0.295

b. Quadratic fit ($y = M_0 + M_1 Z + M_2 Z^2$)

Coefficient	80%	90%	95%
M_0	0.5453	0.6210	0.6745
M_2	−9.535E-3	−9.964E-3	−9.754E-3
M_2	6.494E-5	6.675E-5	6.304E-5

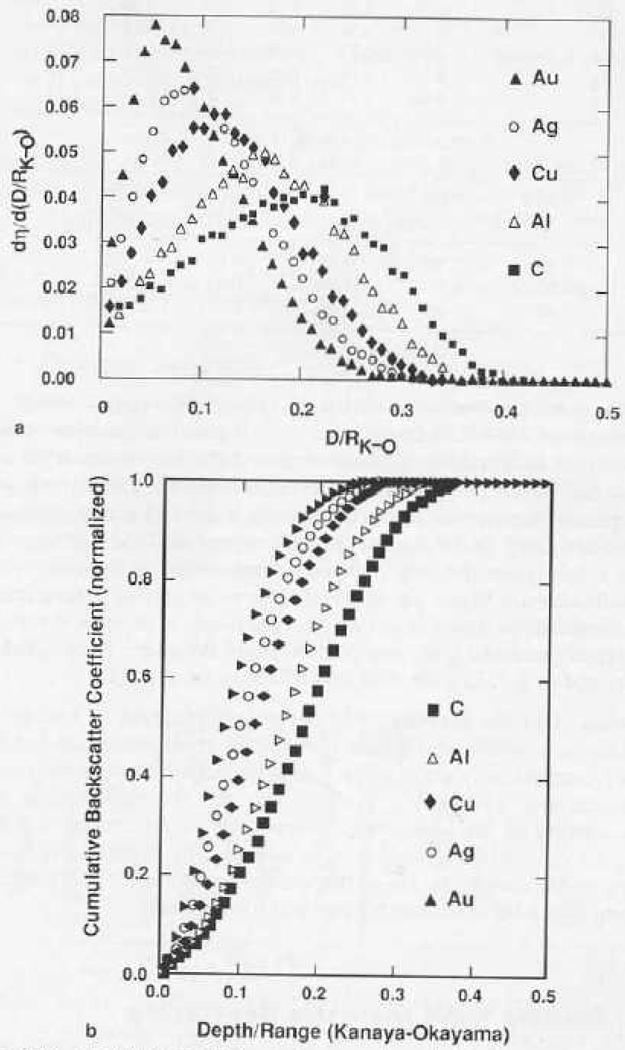

Figure 3.24. (a) Distribution of the maximum depth reached by beam electrons before returning to the surface to escape as backscattered electrons, as calculated by Monte Carlo electron-trajectory simulation. (b) Cumulative backscattering as a function of depth, derived from (a) (Newbury and Myklebust, 1991) $E_0 = 20\,\text{keV}$.

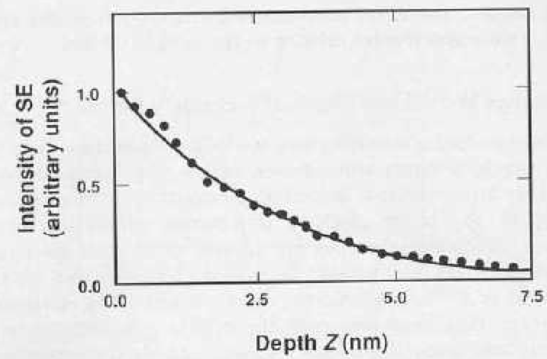

Figure 3.29. Probability of escape of secondary electrons generated at a depth Z below the surface (Koshikawa and Shimizu, 1974).

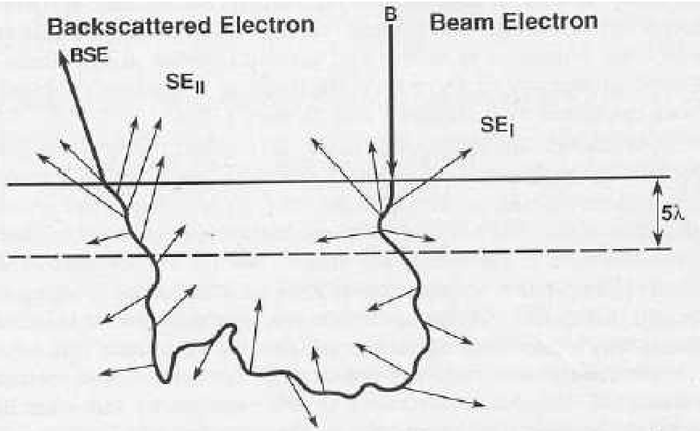

Figure 3.30. Schematic illustration of the origin of two sources of secondary electrons in the sample. Incident beam electrons (B) generate secondary electrons (SE_I) upon entering the sample. Backscattered electrons (BSE) generate secondary electrons (SE_{II}) while leaving the sample. λ is the mean free path for secondary electrons.

TABLE 3.8 SE, BSE yields and ratio of SE produced by primary beam to those generated by BSE.

	δ	η	*SEII / SEI*
Carbon	0.05	0.06	0.18
Aluminium	0.1	0.16	0.48
Copper	0.1	0.30	0.9
Gold	0.2	0.50	1.5

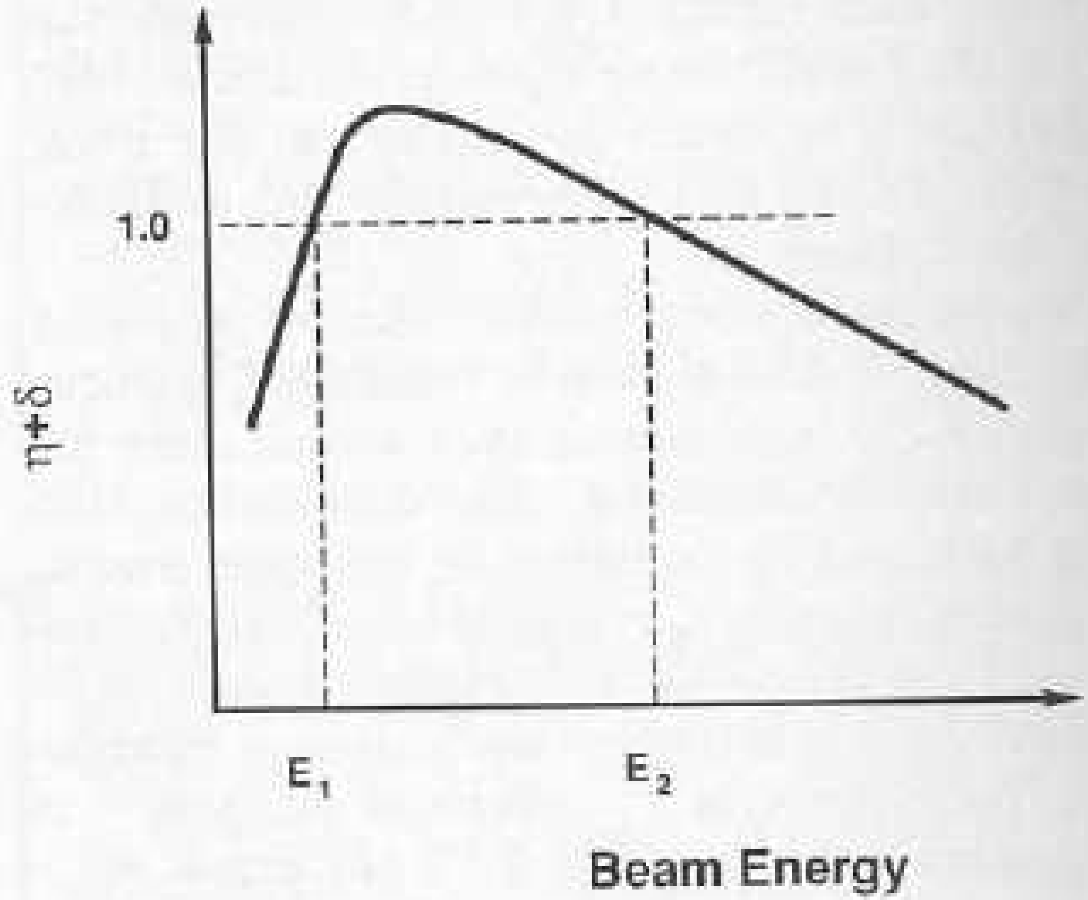

Figure 3.27. Total emitted-electron coefficient $\eta + \delta$ as a function of beam energy.

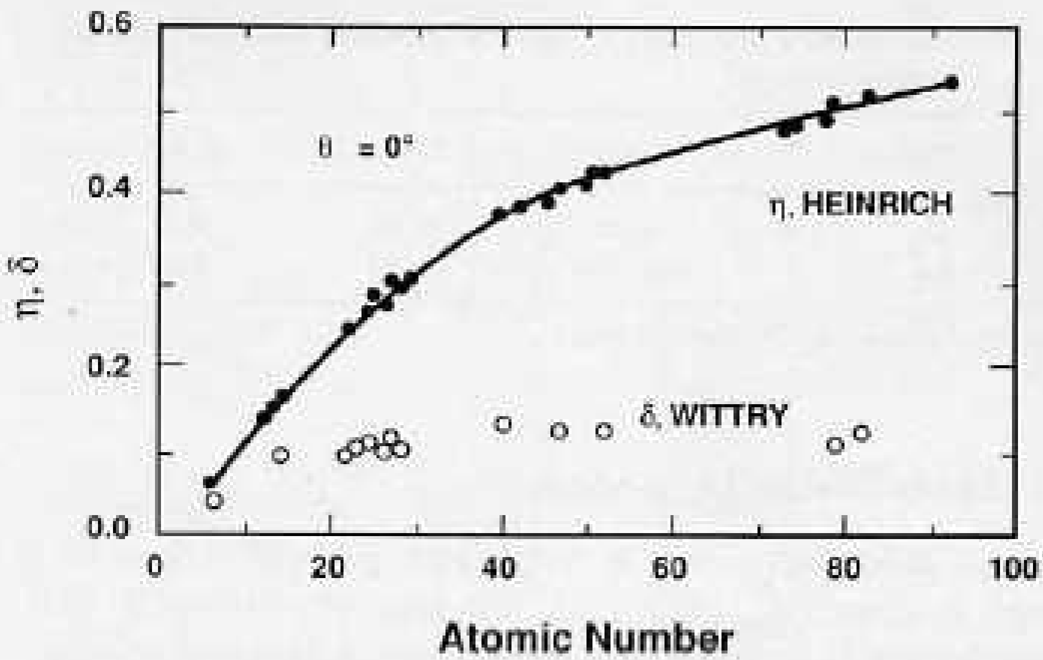

Figure 3.26. Comparison of backscattered-electron and secondary-electron coefficients as a function of atomic number, $E_0 = 30$ keV [data of Wittry (1966) and Heinrich (1966a)].

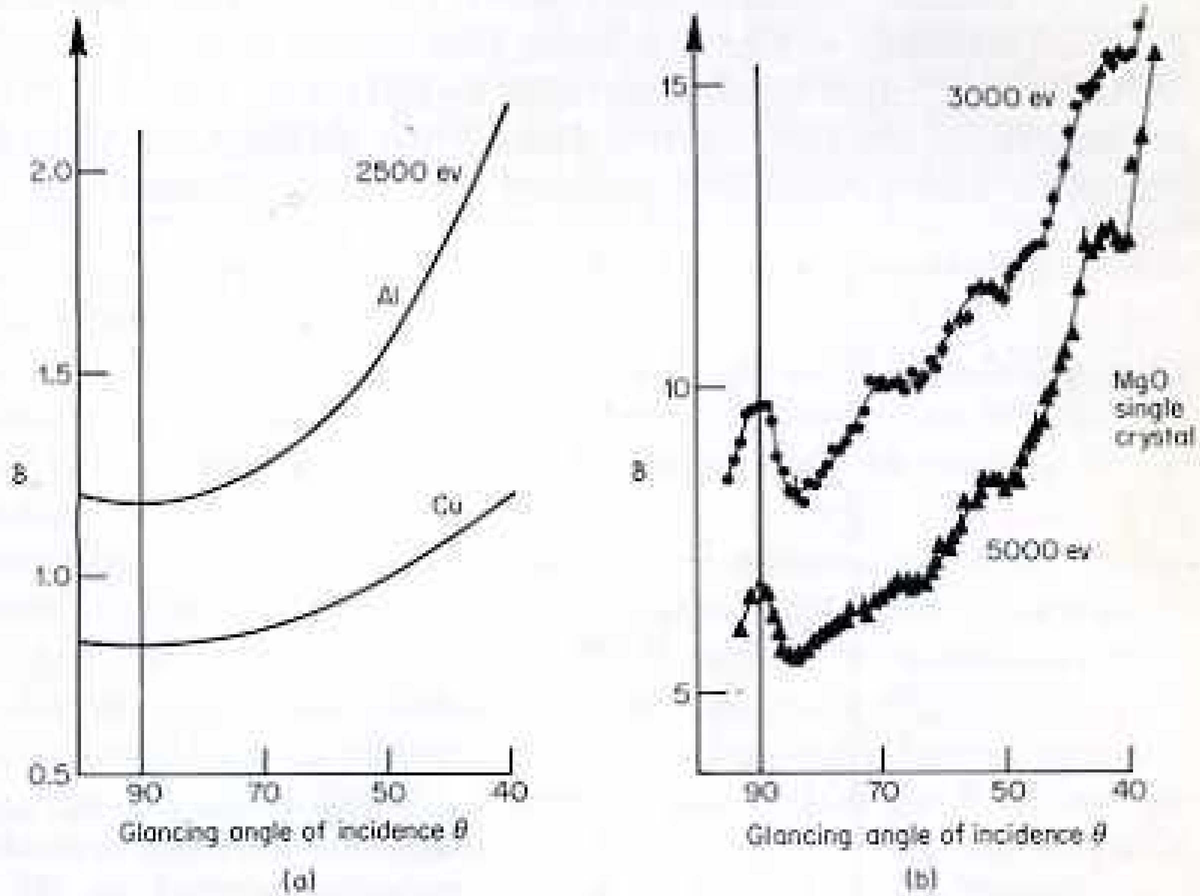

FIG. 3.20 Secondary electron emission versus incident angle. (*a*) For amorphous metals (*Müller 1937. Courtesy of Z. Phys.*); (*b*) for single-crystal MgO. (*Laponsky and Whetten 1960. Courtesy of Phys. Rev. Lett.*)

BACKSCATTERED ELECTRON YIELD (η)

Atomic Number	More or less smooth increase, but $\partial I/\partial z \downarrow$ as Z $\uparrow$
Voltage	Not very sensitive! Range $\uparrow$ as $E_0^{1.7}$, but stopping power $\downarrow$ as $E_0 \uparrow$, i.e., electrons get in deeper (and therefore have a harder time getting out), but having gone in deeper they can undergo more high angle scattering events and get out. These 2 partly cancel one another. *(But remember, that beam intensity as $\uparrow$ voltage $\uparrow$.*
Specimen Tilt	$\eta(\theta)\sim(1 + \cos\theta)^{-P}$, where $P \sim 9/Z^{1/2}$ Small θ (near normal incidence), beam penetrates deep into the sample and path length out of sample is large.
Angular Variation	Path length out of sample, $P=P_0/\cos\phi$. Probability of not being scattered in $P \sim 1/P$ $\eta_\phi = \eta_0 \cos\phi$ *If surface is tilted : Scattered electrons are strongly peaked along direction close to incident direction (influence of forward scattering in Rutherford collisions).*

Energy Distrib"	As Z↑, the fraction of backscattered electrons which have lost only a small amount of energy also increases
Radial Distance	As Z↑, backscattered electrons emerge *laterally* from a zone that is a *smaller fraction* of the total range of penetration (in depth). *Remember: range also ↓ as Z ↑*
Sampling Depth	Same as above. As Z ↑, backscattered electrons emerge from a zone that is a *smaller fraction* of the total range of penetration (in depth). *Remember: range also ↓ as Z ↑.* Thus, signal depth for light elements >> than for heavy ones.

SECONDARY ELECTRON YIELD (δ)

Atomic Number	Insensitive to Z! (Possibly due to the high surface sensitivity and contamination in an SEM vacuum)
Voltage	$\delta\uparrow$ as $E_0\downarrow$
Specimen Tilt	Secant law, $\delta(\theta) \sim \delta_0 \sec\theta$ Unlike BS electrons, secondaries escape from a narrow depth in which the rate of production is ~ constant. As surface is tilted, depth of production rises.
Angular Variation	Displays cos ϕ dependence. Even with a tilted surface *(unlike BS electrons, there is no forward scattering bias; production is isotropic). But remember: δ rises with tilt!*

Element ↓	**kV** →	**5**	**20**	**50**
Aluminium		0.4	0.1	0.05
Gold		0.7	0.2	0.1

LOW VOLTAGE MICROSCOPY

- Backscatter yield can increase for low Z at < 5 kV
- Secondary yield can go beyond unity for insulators and bad conductors. Charging eliminated
- Lateral resolution improves due to reduced backscattering-induced secondaries
- Depth resolution improves substantially due to reduced range. Backscatter and secondary ranges become comparable
- Sensitivity to topography increases substantially
- Beam current drops!! Poor signal! Cannot use W-sources below ~ 5 kV. Need field emission cathodes

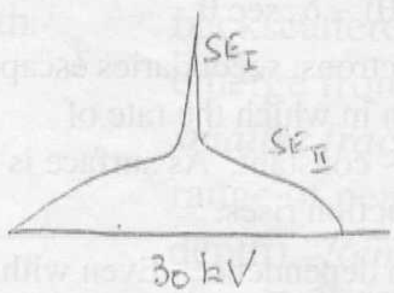

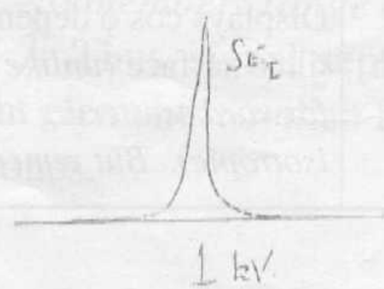

FIG. 6.16 Increase in image contrasts obtained by reducing the accelerating potential. Hydrogen embrittlement crack surface, 18% Ni (250 grade) maraging steel, examined at (*a*) 5 kv; (*b*) 20 kv. (*Pickwick and Smith 1972. Courtesy of Micron.*)

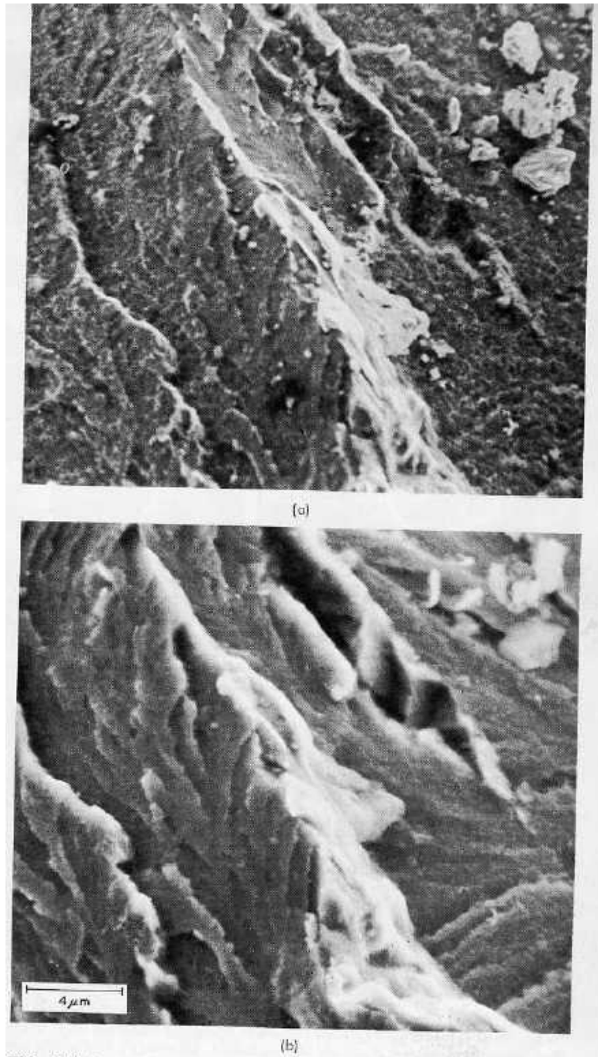

FIG. 6.16 Increase in image contrasts obtained by reducing the accelerating potential. Hydrogen embrittlement crack surface, 18% Ni (250 grade) maraging steel, examined at (*a*) 5 kv; (*b*) 20 kv. (*Pickwick and Smith 1972. Courtesy of Micron.*)

127

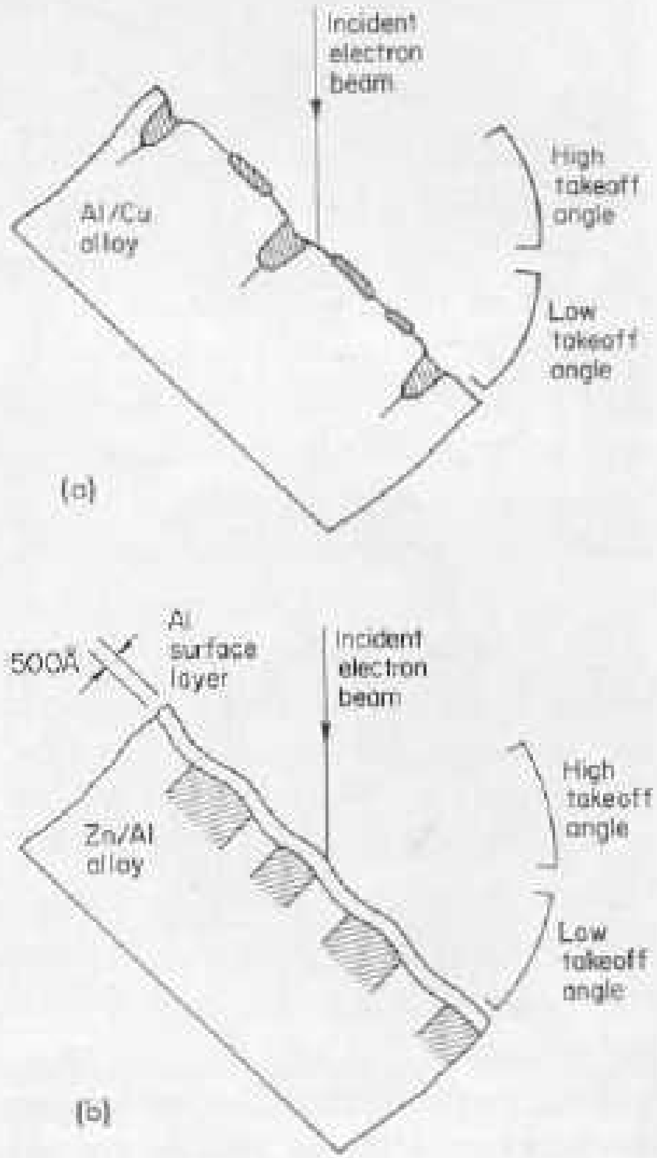

FIG. 6.23 Test samples. (*a*) Large grained sample of Al-Cu alloy having shallow precipitates on the surface and deeper precipitates at the grain boundaries; (*b*) 500-A Al film evaporated onto segregated Zn-Al substrate.

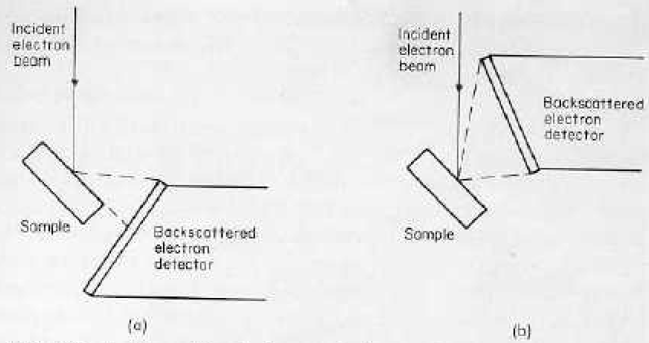

FIG. 6.22 Positions of the backscattered electron detector to give (*a*) low-deflection image and (*b*) high-deflection image of test samples shown in Fig. 6.23.

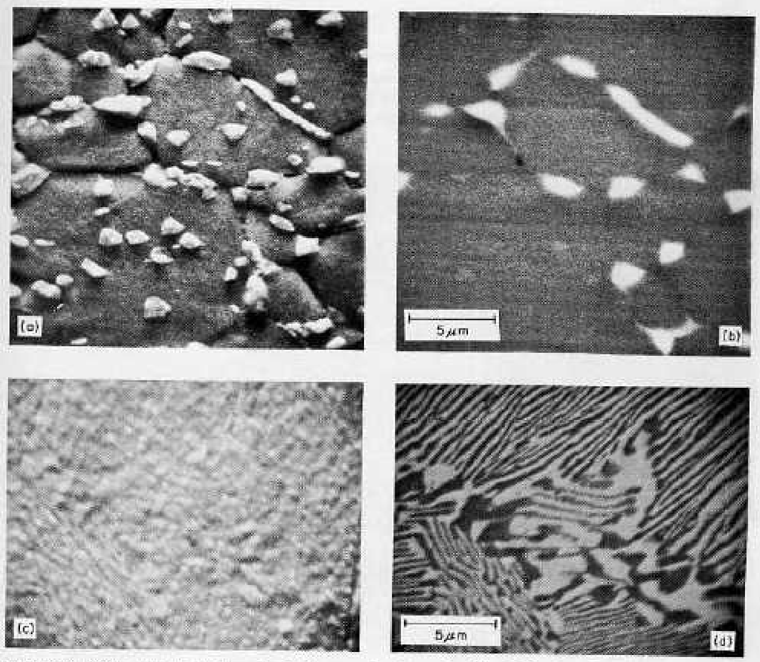

FIG. 6.24 Micrographs obtained with the sample shown in Fig. 6.23 using the collector position shown vertically above.

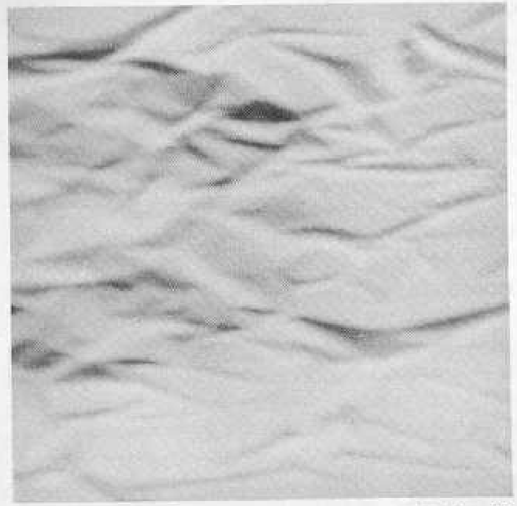

FIG. 6.25 A 2000-Å Cu film over 0.1-cm-diameter hole in solid substrate imaged using solid-state backscattered electron detector with low takeoff angle ($\theta = 45°$; $\theta' = 25°$). (*R. Shimizu and T. Matsukawa unpublished, Dept. of Physics, Osaka Univ.*)

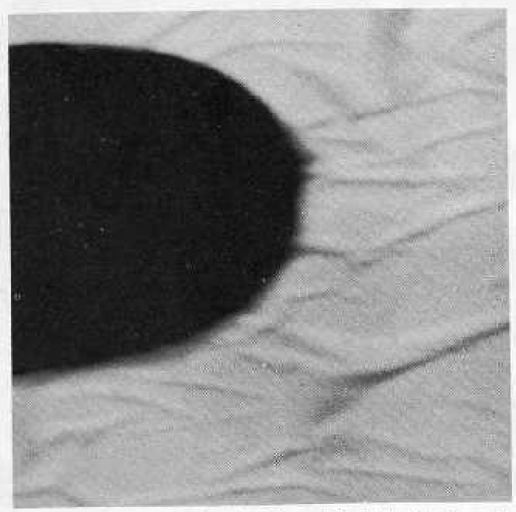

FIG. 6.26 Same as Fig. 6.25 but with high takeoff angle ($\theta = 45°$; $\theta' = 90°$).

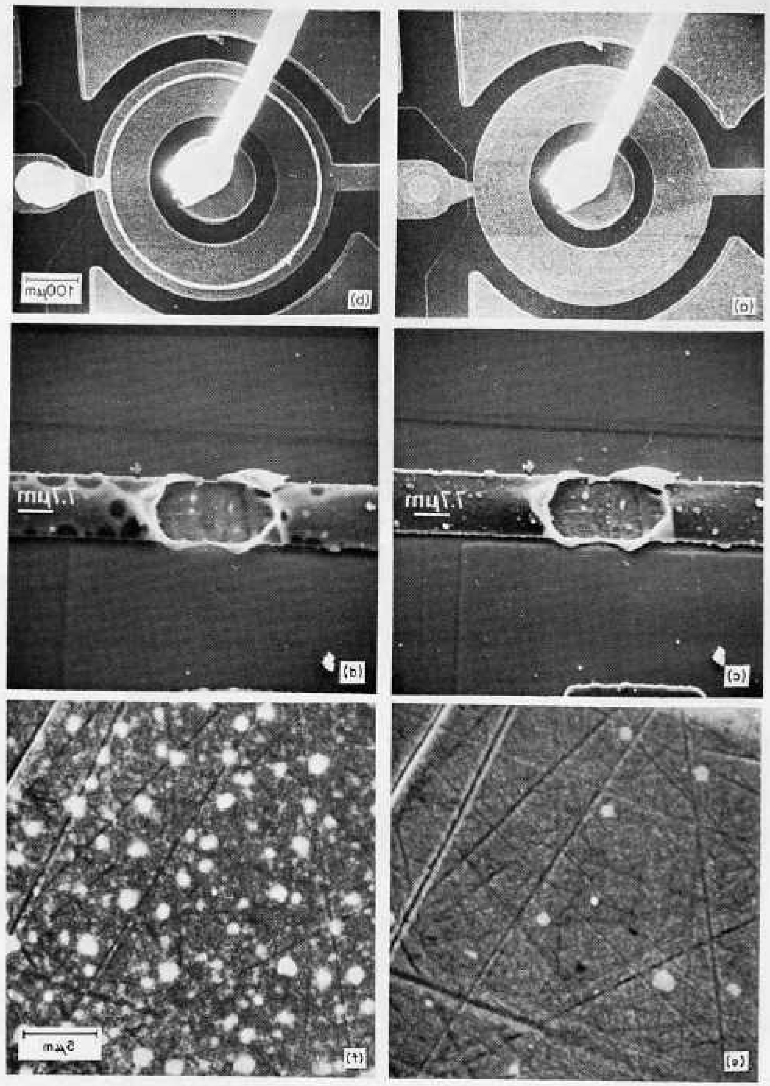

FIG. 6.17 Effect of varying the incident voltage. Insulated gate field-effect transistor viewed at (a) 10 kv; (b) 20 kv. Also, failed aluminum conductor viewed at (c) 10 kv; (d) 20 kv (E. D. Wolf, unpublished, Hughes Res. Lab, Malibu, Calif.). (e) and (f) Al-Cu alloy with precipitates examined at 5 kv and 25 kv (secondary electron image with normal incidence). (P. Beaufrere et al. unpublished, IBM Essonnes Plant, France.)

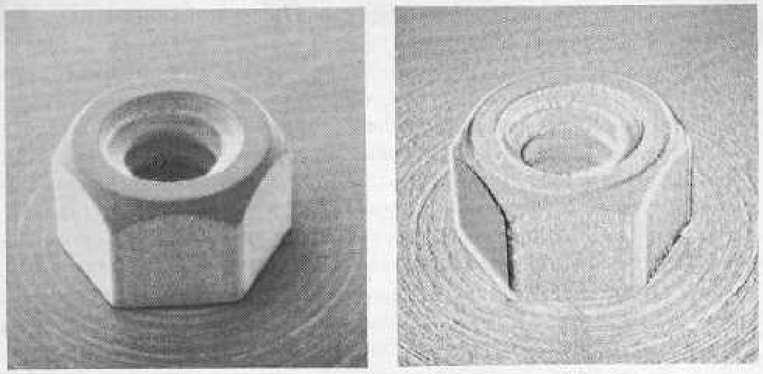

(a) (b)

FIG. 6.1 Secondary electron images of 00–90 brass nut. (*a*) Usual display method; (*b*) with the video waveform differentiated (horizontal scan). Distances between flats = 1.95 mm. All the images in this chapter were obtained by collecting the secondary electrons unless stated otherwise.

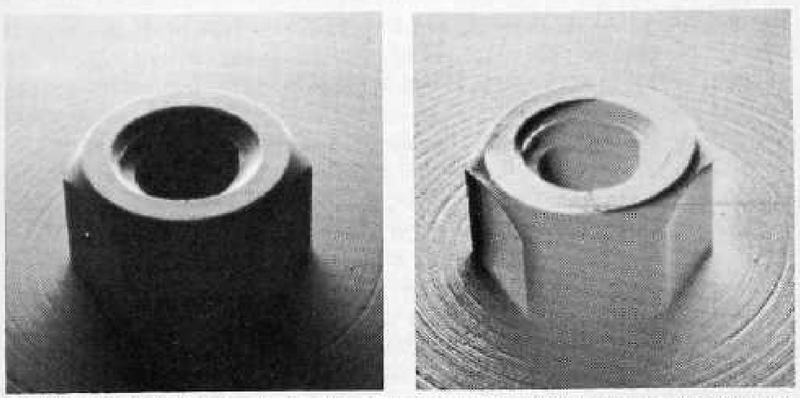

FIG. 6.2 As Fig. 6.1 but the backscattered electron image. Note the blank areas where the surface is shielded from the collector.

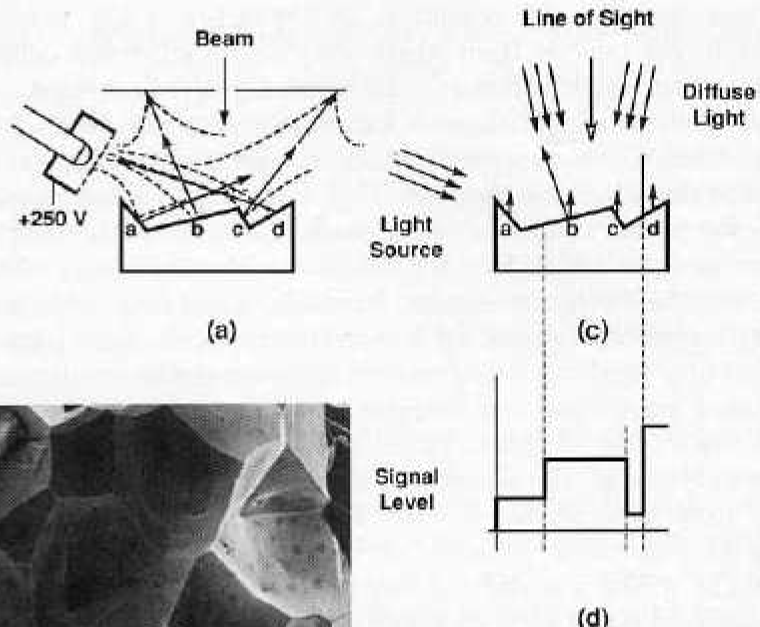

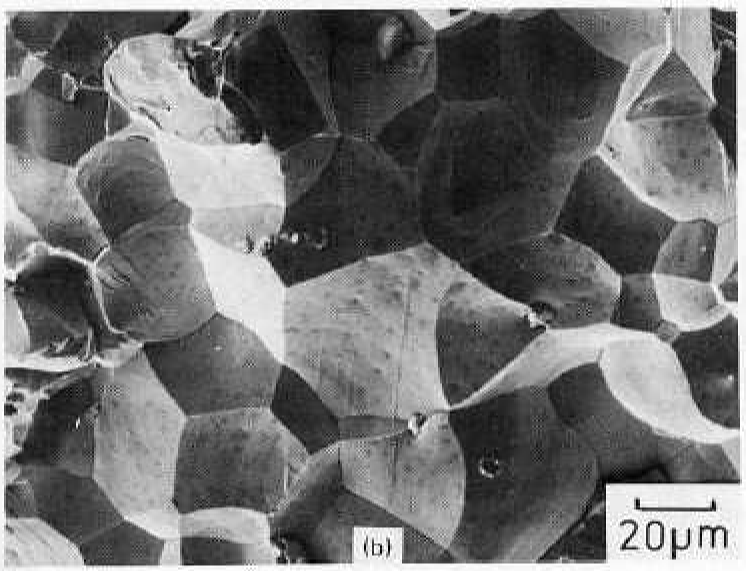

Figure 4.34. (a) Electron collection from randomly oriented surfaces. E–T detector, biased positively. Solid trajectories, backscattered electrons; broken trajectories, secondary electrons. (b) Image of an iron fracture surface with this detector condition; the detector is located at the top of the image; same field as in Fig. 4.33b. (c) Equivalent optical illumination and position of the line of sight to produce a similar image. (d) Schematic of signal as a function of beam position.

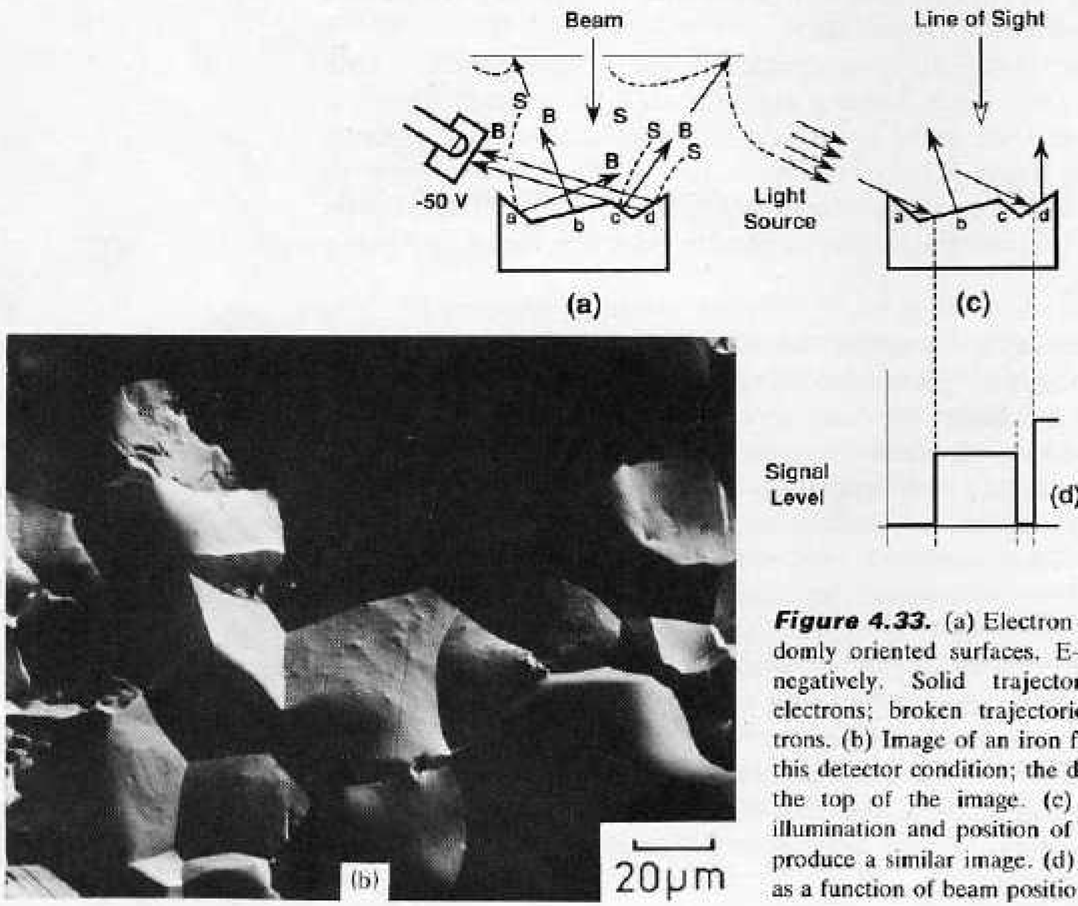

Figure 4.33. (a) Electron collection from randomly oriented surfaces. E–T detector, biased negatively. Solid trajectories, backscattered electrons; broken trajectories, secondary electrons. (b) Image of an iron fracture surface with this detector condition; the detector is located at the top of the image. (c) Equivalent optical illumination and position of the line of sight to produce a similar image. (d) Schematic of signal as a function of beam position.

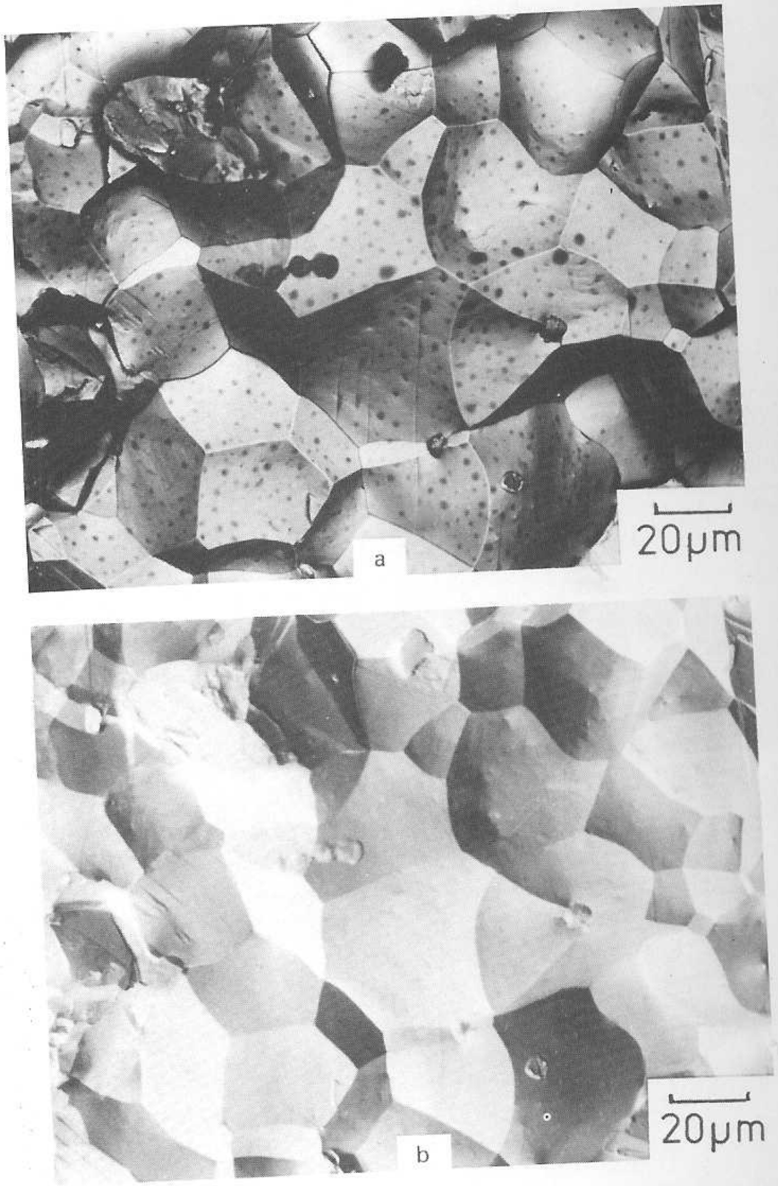

... Figs. 4.34 and 4.35, but view...

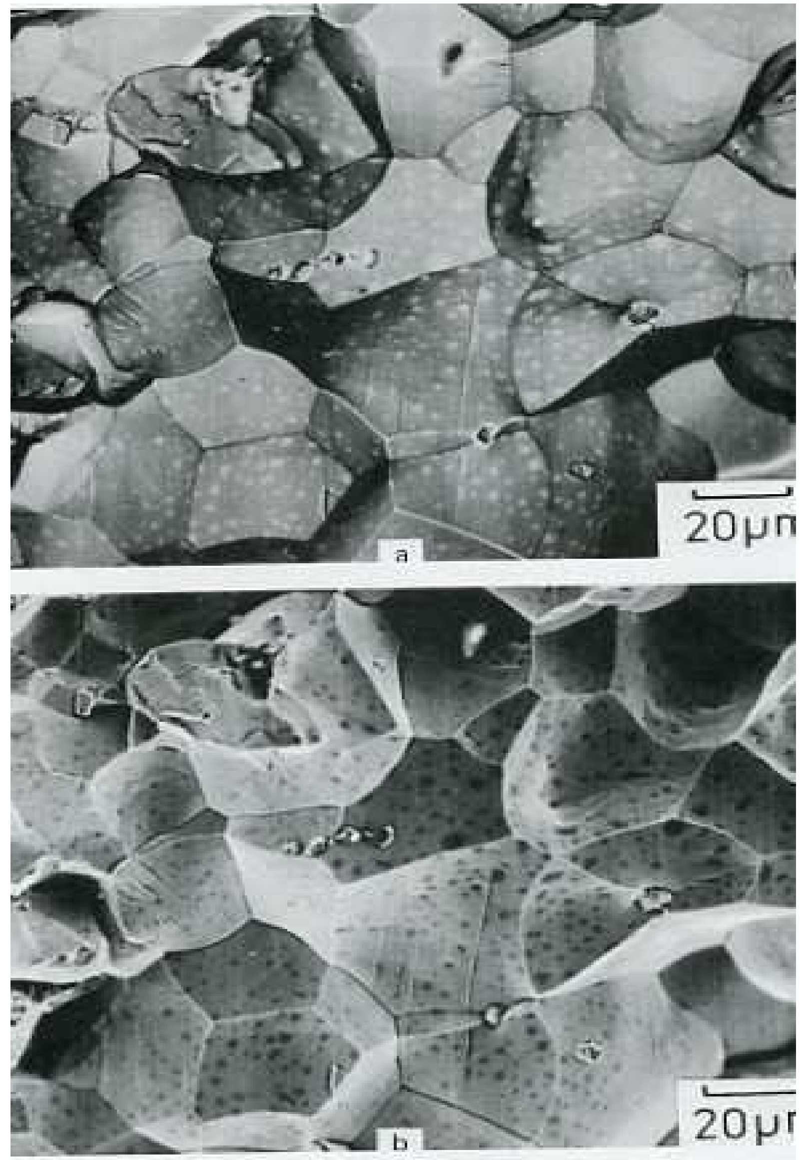

Figure 4.37. (Continued).

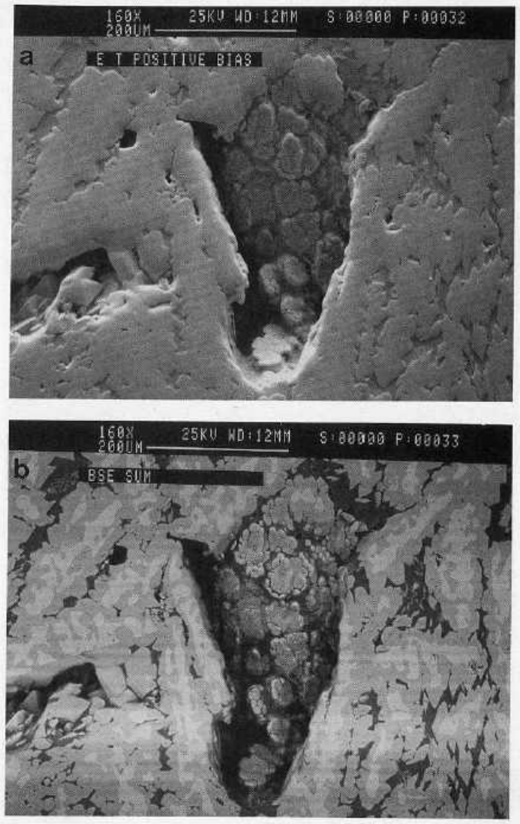

Figure 4.38. Separation of contrast components. The specimen is Raney nickel, which

Figure 4.38. Separation of contrast components. The specimen is Raney nickel, which contains multiple phases that produce atomic number contrast and surface defects that produce topographic contrast. (a) The specimen is viewed with a positively biased E–T detector, showing predominantly topographic contrast. (b) Four-quadrant solid-state BSE detector, sum mode: atomic number contrast dominates the image. (c) Difference mode, TOP – BOTTOM: topographic contrast dominates, with apparent top illumination. (d) Difference mode, BOTTOM – TOP: topographic contrast dominates, with apparent bottom illumination. (e) Difference mode, RIGHT – LEFT: topographic contrast dominates, with apparent illumination from the right. (f) Difference mode, LEFT – RIGHT: topographic contrast dominates, with apparent illumination from the left.

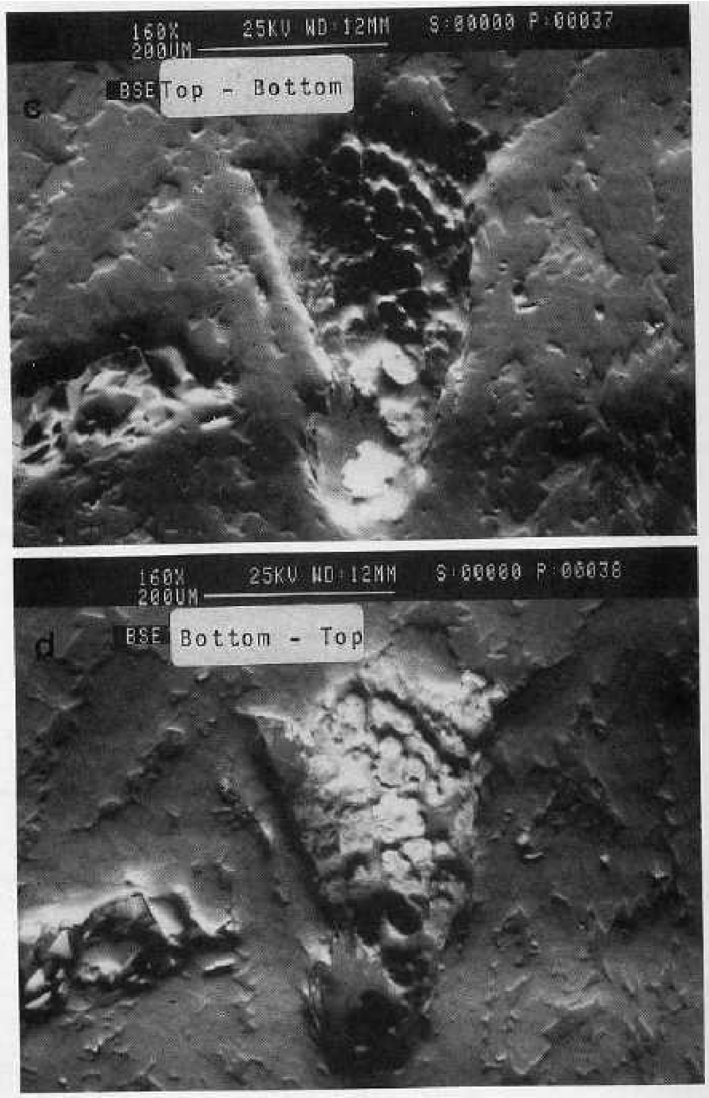

Figure 4.38. (Continued)